Correlative Multi-scale Imaging of Shales: A Review and Future Perspectives

Ma, Lin[1,2], Fauchille, Anne-Laure[1,3], Dowey, Patrick J. [2], Figueroa Pilz, Fernando[1,3], Courtois, Loic[1,3], Taylor, Kevin G.[2*],Lee, Peter D.[1, 3],

[1]Manchester X-ray Imaging Facility, School of Materials, University of Manchester, Manchester, M13 9PJ, UK

[2] School of Earth and Environmental Sciences, University of Manchester, Manchester, M13 9WJ, UK

[3]Research Complex at Harwell, Rutherford Appleton Laboratory, Harwell, Oxfordshire, OX11 0FA, UK

*** Corresponding author**

Abstract:

As the fastest growing energy sector globally, shale and shale reservoirs have attracted the attention of both industry and scholars. However, the strong heterogeneity at different scales and the extremely fine-grained nature of shales makes macroscopic and microscopic characterisation highly challenging. Recent advances in imaging techniques have provided many novel characterisation opportunities of shale components and microstructures at multiple scales. Correlative imaging, where multiple techniques are combined, is playing an increasingly important role in the imaging and quantification of shale microstructures (for example, one can combine optical microscopy, SEM/TEM and X-ray radiography in 2D, or XCT and 3D-EM in 3D). Combined utilization of these techniques can characterize the heterogeneity of shale microstructures over a large range of scales, from macroscale to nanoscale (~10^0 - 10^{-9} m). Other chemical and physical measurements can be correlated to imaging techniques to provide complementary information for minerals, organic matter and pores. These imaging techniques and subsequent quantification methods are critically reviewed to provide an overview of the correlative imaging workflow. Applications of the above techniques for imaging particular features in different shales are demonstrated and key limitations and benefits summarized. Current challenges and future perspectives in shale imaging techniques and their applications are discussed.

Keywords: shale, correlative imaging, quantification, multi-scale, microstructure, microscopy, X-ray computed tomography,

Shales are widespread in sedimentary basins, and unconventional shale-gas and shale-oil reservoirs are playing an increasingly important role in oil and gas production globally (EIA 2015). Technological advances in horizontal drilling and hydraulic fracturing have greatly promoted their exploitation (Curtis *et al*. 2010; Clarkson *et al*. 2012; EIA 2015). Shales are also important in carbon sequestration (Chadwick *et al*. 2004) and as potential repositories for nuclear waste (Mallants *et al*. 2001; Bossart and Thury 2007).

The integrated characterization of shale reservoir properties is critical for improved reservoir prediction and enhanced recovery; however, the extremely fine-grained nature of shales makes precise quantification challenging (Sondergeld *et al*. 2010a; Chiou *et al*. 2012). Advanced imaging and image-based quantification techniques have become a key solution for the macroscopic and microscopic characterisation of shale reservoirs (Curtis *et al*. 2012). Traditional two-dimensional (2D) imaging techniques such as optical microscopy (OM) and scanning electron microscopy (SEM) have proved the feasibility of imaging microstructures in single planes (Krinsley et al. 1983; Milner et al. 2010b; Klaver et al. 2012). Other techniques including X-ray radiography and transmission electron microscopy (TEM) further expand the spatial scales and image resolutions that can be achieved (Algeo *et al*. 1994; Bernard *et al*. 2013a). To provide morphological and topological information on fine-grained components, three-dimensional (3D) imaging techniques such as X-ray computed tomography (XCT) and 3D electron microscopy (EM) have been used in many shale plays (Sok *et al*. 2010; Keller *et al*. 2013b; Ma *et al*. 2016).

Key features in shales include fractures, pores, organic matter and minerals; and these are highly heterogeneous on a range of scales. Multi-scale image analysis has the potential to significantly improve geological models in these systems (Ross and Bustin 2009; Sondergeld *et al*. 2010b; Slatt 2011). Used in isolation, each imaging technique has particular applications and limitations. 2D imaging techniques are generally easier to access but cannot provide information on the spatial distribution and connectivity of shale components (Klaver *et al*. 2015). Large SEM image mosaics at high resolutions can be acquired on shales to provide representative mineral phase distributions and capture mineralogical heterogeneities (Fauchille *et al*. 2014). XCT can provide 3D images of core samples but cannot resolve below 50 nm (Withers 2007; Landis and Keane 2010). 3D- EM can be used to image pores and clay minerals at the nanometre scale but cannot provide a large field of view of microscale structures (Curtis *et al*. 2012; Zhang *et al*. 2012).

Because of the above limitations, correlative imaging at multiple scales becomes necessary to observe and quantify features in shale studies. The use of multiple scales and techniques has recently been explored by a number of authors (Keller *et al*. 2013b; Hemes *et al*. 2015; Ma *et al*. 2016). The aims of this review are threefold: (i) To critically review 2D and 3D imaging techniques; (ii) to outline how these techniques have been applied to shales to answer fundamental questions on textures and

structure; and (iii) to present future challenges and how new developments and approaches may be applied to address these challenges.

Nature of shales and shale reservoirs

Shale components

Shale has been widely used as a class name for all fine-grained sedimentary rocks, and is defined as a rock in which more than fifty percent of its grains are mud (clay and silt) size (< 62.5 μm) (Lazar *et al*. 2015). Many shales contain 20 to 60 wt % of clay minerals and 10 to 50 wt% of non-clay grains (Schultz 1964; Shaw and Weaver 1965; Schmitt *et al*. 1994; Savoye *et al*. 2001). The proportion of organic matter in shales can be highly variable and depends on a number of factors including geological setting, depositional environment and diagenetic environment during formation. Organic matter provides the source for hydrocarbons in shale reservoirs. Shale microstructure is typically complex, heterogeneous and anisotropic, and can be used to identify sedimentary depositional environments and analyse diagenetic processes (Chiou *et al*. 2012; Potter *et al*. 2012). Micro- to nano-scale pores in shales provide hydrocarbon storage capacity, while naturally occurring fractures can improve the permeability of the reservoir (Curtis 2002; Sondergeld *et al*. 2010a).

Mineral composition

Shale mineral components can include carbonates (e.g. calcite, dolomite), tectosilicates (e.g. quartz, feldspar), phyllosilicates (e.g. illite, smectite, kaolinite, interlayers illite/smectite), sulphides, oxides, and phosphates (Yaalon 1961; Foscolos *et al*. 1976; Ross and Bustin 2009). The proportions of each mineral vary significantly because of different sedimentary and maturation conditions (Potter *et al*. 2005; Lazar *et al*. 2015).

The composition and distribution of these components not only indicate which sedimentary and diagenetic processes formed these shales, they also play a primary role in defining rock properties. Distinction and quantification of clay minerals from non-clay minerals is important as both have very different mechanical behaviours due to their structure, morphology and chemical composition.

Shales with a high concentration of clay minerals have relatively high specific surface areas and low permeability (Pusch 2006). Non-clay mineral grains (rigid inclusions) can also affect the fluid transport and mechanical properties of the rock (Horseman *et al*. 1996; Vasin *et al*. 2013).

Organic matter

Organic matter is present in oil- and gas-bearing shales. Organic matter particle size varies significantly in different shale reservoirs, from a few nanometres to hundreds of microns (Curtis *et al*. 2014). Sufficient organic matter content, appropriate kerogen compositions and adequate thermal

maturity are necessary for organic matter in shales to mature and form hydrocarbons (Tissot *et al*. 1974; Bernard and Horsfield 2014). Organic matter concentration in shales is described using the chemical measurement of evolved total organic carbon (TOC). Shale gas/oil plays are normally rich in organic matter, with a TOC greater than 2% (Tissot 1984; Gasparik *et al*. 2014). Reservoir maturity is described through either optical microscope observation (eg. vitrinite reflectance, R_O) or pyrolysis measurements (eg. T_{max}) (Vassoyevich *et al*. 1970; Tissot *et al*. 1987). Productive shale gas/oil plays are normally mature with Ro > 1.2% and Tmax > 465° C (Jarvie *et al*. 2007; Bernard and Horsfield 2014). Organic matter compositions also influence shale gas/oil production (Curtis *et al*. 2011a; Sondergeld *et al*. 2013). The solubility of organic matter in the presence of organic solvents defines the type of organic matter: insoluble kerogen and soluble bitumen (Curtis *et al*. 2011a). Kerogen is further divided into four types (I, II, III and IV) based on the relative proportion of hydrogen relative to carbon and oxygen (Tissot *et al*. 1974).

Pores

In shales, pores provide the majority of gas and oil storage space and surface areas for gas adsorption. The network of pores is the key parameter for fluid transport (Bustin *et al*. 2008). Shale reservoirs typically have pores ranging in size from a few nanometres to a few microns (Javadpour 2009; Clarkson *et al*. 2013; Jiao *et al*. 2014), this is typically one thousandth to ten thousandth the size of pores found in a conventional reservoir. A three-category classification of pore sizes is widely used in shale reservoirs: macropores (>50 nm), mesopores (2–50 nm) and micropores (<2 nm) (IUPAC 1994).

Pores in shales are of three main forms: mineral matrix pores (including interparticle pores and intraparticle pores), organic matter pores (pores within or around organic matter) and fracture porosity (Slatt and O'Brien 2011; Loucks *et al*. 2012; Zhang *et al*. 2012). Micropores and mesopores are present mostly in organic matter and clay mineral-rich shale. Macropores are commonly reported between mineral grains in silica-rich or carbonate-rich shales (Reed and Loucks 2007; Loucks *et al*. 2009; Kuila and Prasad 2013).

Intraparticle pores are often located within carbonate phases such as dolomite and calcite, but are also present in pyrite, chlorite and micas. Most small pores (mesopores and micropores) are interparticle pores within clay minerals (for example inside swelling clay mineral particles such as the interstratified illite/smectite) or organic matter pores (Sammartino *et al*. 2002; Yven *et al*. 2007; Curtis *et al*. 2010; Kuila and Prasad 2013; Klaver *et al*. 2015). However, larger pores (30 nm to 100 nm diameter) within organic grains have also been reported in the Mississipian Barnett Shale (Loucks *et al*. 2009). Pore morphologies and sizes are related to mineralogy (Loucks *et al*. 2012), and can change at different scales because of depositional and burial diagenetic history (Chiou *et al*. 2012).

Gas is generally stored in shale reservoirs in three forms: (i) free gas in micro- or nano-pores between or within minerals, (ii) adsorbed gas on the surface of pores in or around organic matter and clay

minerals and (iii) gas dissolved in kerogen bodies (Curtis 2002; Etminan *et al*. 2014). Gas transport modes differ with pore sizes (Knudsen 1934; Roy *et al*. 2003; Sondergeld *et al*. 2010c). Darcy flow is considered to dominate in macropores such as fracture porosity in shale reservoirs. In mesopores flow enters the Knudsen regime, where molecular collisions with pore walls, adsorption and Brownian flow become important (Javadpour *et al*. 2007; Sondergeld *et al*. 2010c; Shi *et al*. 2013).

Within a solid material, volumetric porosity is the ratio between the volume of void space and the bulk volume of the material. The voids or pores can be filled with fluids (liquid or gas), and are either connected or unconnected (Bear and Braester 1972). Porosity in shale reservoirs typically ranges from 2 to 15% (Chalmers *et al*. 2012; Klaver *et al*. 2015). Porosity can be measured using helium porosimetry, mercury intrusion porosimetry (MIP), gas adsorption, water adsorption and calculated in 2D through image analysis on SEM and focused ion beam-scanning electron microscopy (FIB-SEM) (Heath *et al*. 2011b; Chalmers *et al*. 2012; Mastalerz *et al*. 2012; Schieber *et al*. 2012; Clarkson *et al*. 2013; Klaver *et al*. 2015).

Microstructure and anisotropy of shales

Shale microstructure, including the morphology, arrangement and distribution of components, can be used to identify the sedimentary environment of deposition and processes which altered the shale during diagenesis (Chiou *et al*. 2012). Microstructure can be characterised using various property measurements including component (minerals, organic matter and pores) volume fractions, orientations and connectivity (Kaarsberg 1959; Tosaya 1982; Sayers 1994). The anisotropy of shales is likely to be controlled principally by depositional setting (Day-Stirrat *et al*. 2010) and can be produced during bioturbation and cementation in early diagenesis (Milliken and Day-Stirrat 2013).

In shales, phyllosilicates (clay minerals) can acquire a preferred bedding-parallel orientation during sedimentation and compaction (Sayers 1994). Additionally, dissolution of smectite and precipitation of illite can also result in the anisotropy (Aplin *et al*. 2006; Day-Stirrat *et al*. 2008). Recent studies have shown that non-clay mineral grains (eg. carbonates, quartz) may also have elongated shapes with bedding-parallel orientation (Klaver *et al*. 2012; Robinet *et al*. 2012; Vasin *et al*. 2013; Fauchille 2015). Pores and kerogen structures have also been reported with strongly anisotropic and complex features (Sayers 1994; Vasin *et al*. 2013); however in some shales no specific preferred orientation is observed (Slatt and O'Brien 2011).

The different mechanical and physical properties of shales (i.e. permeability, hydraulic and electrical conductivities, elasticity, strength) in various orientations are often controlled by the direction of bedding planes and the microstructural anisotropy (Hornby 1998; Pham *et al*. 2007; Sarout and Guéguen 2008; Hedan *et al*. 2012; Vasin *et al*. 2013; Hedan *et al*. 2014; Cosenza *et al*. 2015a; Cosenza *et al*. 2015b; Bonnelye *et al*. 2016b, a; Fauchille *et al*. 2016). To fully understand the

microstructure of shales, the application of either 2D or 3D imaging in several orientations is required (Milner et al. 2010b; Sondergeld et al. 2010a).

History and principles of multi-scale imaging techniques in shales

Definition of multiple scales

Shales are heterogeneous on a wide range of scales (Hornby 1998; Sammartino *et al*. 2002; Giraud *et al*. 2007; Ortega *et al*. 2007; Bobko and Ulm 2008; Robinet *et al*. 2012; Cariou *et al*. 2013). Therefore, qualitative and quantitative information on compositional and textural features requires a multi-scale and correlative imaging approach as shown in Figure 1. Correlative imaging consists of using different imaging modalities such as electron microscopy with X-ray tomography and then combining the results to obtain greater insights. Multi-scale characterization of shales consists of taking images at various scales at different resolutions. For accurate and representative characterization of all shale features, it is essential to consider which features are resolvable at each scale. It is also important to consider how each feature can be related over the range of scales. For example the quantification of the length and aperture of natural fractures (eg. 10^{0} - 10^{-3} m) requires different sampling strategies, sample preparations, analytical techniques and data analyses than the study of porosity (eg. 10^{-8} to 10^{-9} m) within the same sample.

There is an inherent scale hierarchy in shales which can be recognized due to their heterogeneity. These scales are defined here and, as outlined below, consist of: macroscale, mesoscale, microscale, low-resolution nanoscale, and high-resolution nanoscale.

The macroscale refers to the length scale of 10^{-3} m or larger. Natural fractures, lithofacies and bedding or lamina information can be observed at the macroscale (Ortega *et al*. 2010; Kumar *et al*. 2012; Torsaeter *et al*. 2012). At the mesoscale (10^{-3} to 10^{-5} m length scale), fractures are still visible, and it is possible to differentiate between the homogeneous matrix and more heterogeneous large non-clay mineral grains (Silin and Kneafsey 2012; Houben *et al*. 2014). At the microscale (10^{-5} to 10^{-6} m length scale) sedimentological textures can be imaged and quantified; and the distribution of silt-size minerals grains and organic matter can be imaged (although this is still grain size dependent) (Sakellariou *et al*. 2003; Lemmens and Butcher 2011). At the low-resolution nanoscale (10^{-6} to 10^{-7} m length scale), large silt-sized mineral grains cannot be resolved but organic matter and clay minerals distributions can be visualised (Gelb *et al*. 2011; Bin *et al*. 2013). At the high-resolution nanoscale (10^{-8} to 10^{-9} m length scale) the majority of pores can be imaged, and the spatial relationship of pores to minerals or organic matter can be analysed (Reed and Loucks 2007; Tariq *et al*. 2011; Bernard *et al*. 2013b).

Although difficult it is possible, through multi-scale characterization, to image the same area or

volume across two or more scales. 2D SEM mosaics were used to characterize the non-clay grains structure at the millimetre scale (Robinet *et al*. 2012; Fauchille *et al*. 2014), and the pore structure at the micron scale (Klaver *et al*. 2012; Houben *et al*. 2014). However in 3D, it is difficult to cover a large range of scales due to the large numbers of subvolumes at lower scales to cover the whole volume.

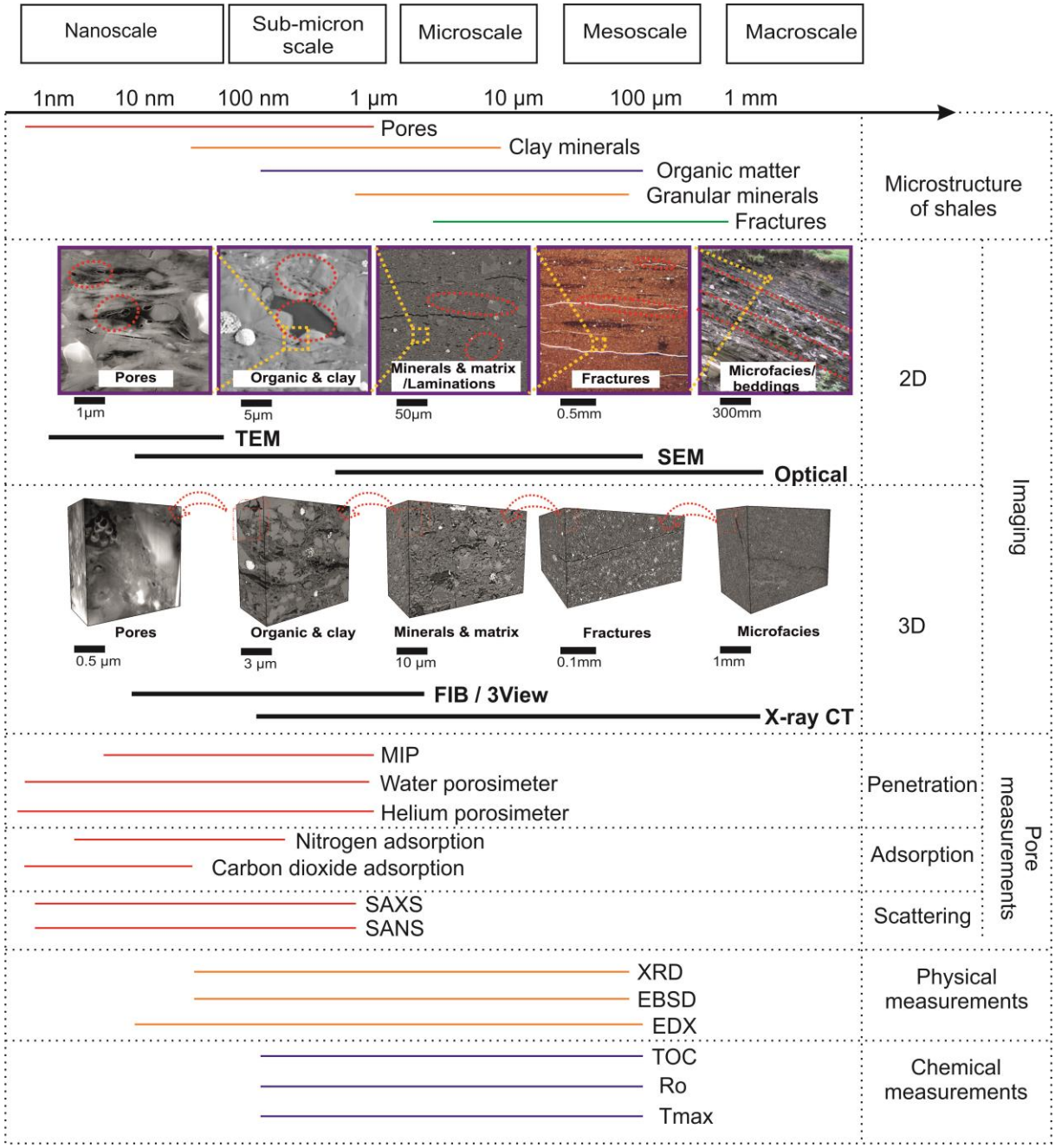

Figure 1 Scales and techniques used in correlative multi-scale imaging of shales.

2D imaging techniques

The most common techniques used for 2D imaging of shales are optical microscopy (OM), electron microscopy (EM) including scanning electron microscope (SEM) and transmission electron microscopy (TEM), and X-ray radiography.

Shale microstructure observations require careful sample preparation. For OM and SEM observations, the surface investigated should be extremely flat and well-polished. This prevent artefacts obscuring the sample, reduces image blurring caused by high surface relief and allows high quality atomic number contrast on SEM images (Krinsley *et al*. 2005). Sample impregnation with resin followed by sample cutting and mechanical polishing of the thin section surface is the most common way to obtain a flat surface. However other preparation methods and products can be used to produce sample with different qualities. The impregnation of samples with polymethyl methacrylate (PMMA) resin can significantly improve the quality of petrographic images by preserving the texture without losing the clay confinement or modifying the pore space geometry during sample manipulation (Sardini *et al*. 2009; Prêt *et al*. 2010a; Prêt *et al*. 2010b; Gaboreau *et al*. 2016). Due to its fissility cutting shale samples for image analysis can be difficult, and because of the typically very low permeability of shales, resin impregnation can be slow (Prêt 2003; Jorand 2006; Prêt *et al*. 2010a; Prêt *et al*. 2010b; Gaboreau *et al*. 2011; Robinet *et al*. 2012; Gaboreau *et al*. 2016).

After mechanical polishing, ion bean polishing can significantly improve the quality of the sample polish providing a smoother, lower relief surface (less than 20nm side damage) and minimising curtaining effects. This allows very high-resolution imaging at the nanoscale (Milner et al. 2010b; Sondergeld et al. 2010a; Klaver et al. 2015), enabling quantification of very small shale pores (Loucks *et al*. 2009; Klaver *et al*. 2012).

Optical microscopy (OM)

OM has been used to image shales since at least the early 20th century, with the imaging of kerogens, fossils and minerals in oil shales (Conacher 1917; Trager 1924). OM consists of observing thin sections in reflected or transmitted light (polarized). Criteria such as pleochroism, birefringence colour, relief and cleavages, allows large components in shales to be identified. OM provides significant textural information on relatively large areas when compared with higher resolution techniques. Using OM, centimetre- to millimetre-scale textural information and silt-size detrital or authigenic minerals can be observed (Pisciotto 1981; Loucks and Ruppel 2007). In some organic-rich shale samples, microscale kerogen pieces can be imaged and the types and distribution defined (Trager 1924; Buchardt and Lewan 1990). Furthermore, an optical microscope is quick, cheap and accessible to most geoscientists who will also be familiar with its operation from their undergraduate teaching. But at the millimetre scale, microscale and nanoscale components such as individual clay mineral particles and nanopores cannot be resolved. In spite of its relatively low-resolution and

difficulties in image analysis in shales at this scale, OM is still widely used in shale studies, often combined with other high resolution imaging techniques.

Additionally, confocal laser scanning microscopy (CLSM) has showed the potentials in shale studies. A point light source is used to scan the thin section and excite fluorescence in the focal plane. It has been used for kerogen imaging particularly in organic-rich shale samples (Nix and Feist-Burkhardt 2003).

Scanning electron microscopy (SEM)

Using SEM, higher-resolution details of shale microstructure can be observed (Gipson Jr 1965), both in secondary electron (SE) and back-scattered electron (BSE) modes. SE imaging produces an image of the surface topography (Suganuma 1985; Sealy *et al*. 2000). This is particularly useful in imaging the pores in shales where the structures, types, sizes and distributions of pores can be observed and measured (Timur *et al*. 1971; Suganuma 1985; Milliken *et al*. 2013; Klaver *et al*. 2015) (Figure 2 a). BSE image intensity (or grey level) corresponds to a mean chemical composition (Donovan *et al*. 2003), and the BSE mode can also elucidate compositional variability (Scrivener and Pratt 1983; Agar *et al*. 1989) (Figure 2 b). While standard SEM imaging requires a vacuum (10^{-5}-10^{-6} mbar), environmental-SEM (ESEM) allows humid conditions and gaseous water chambers to observe shales in hydrous states (Nix and Feist-Burkhardt 2003). The SEM provides micro- to nano-scale images of shales, and is the most common imaging technique for shale studies due to the need for widening the fields of view and high image resolution (Milliken and Curtis 2016).

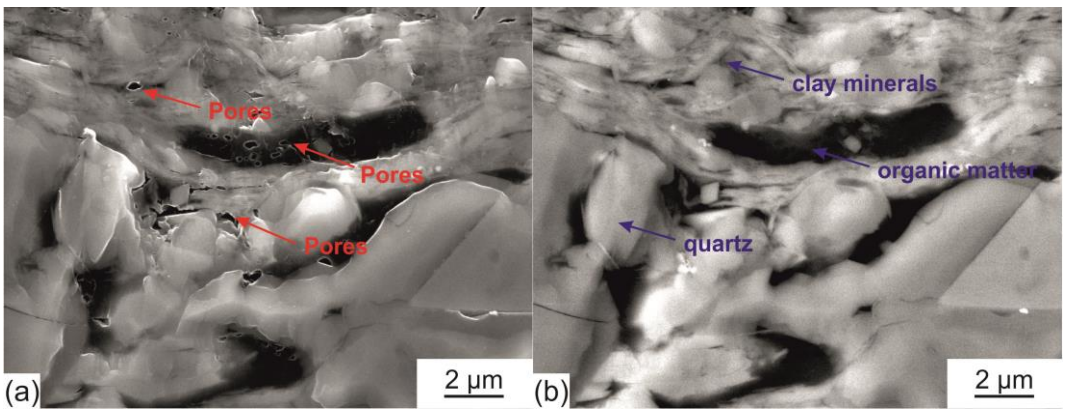

Figure 2 An example of SE and BSE images of same areas in Haynesville shale. (a) The SE image shows surface topography, (b) The BSE image shows mineral compositional.

Transmission electron microscopy (TEM)

TEM produces images through the use of an electron beam that transmits through an ultra-thin sample, hitting a detector on the other side (Curtis *et al*. 2011b). Minerals with low intensity are shown as bright areas and those with high density are shown as dark areas (Chalmers *et al*. 2012; Rodriguez *et al*. 2014). TEM can provide micrometre to sub-nanometre sized images of clay minerals (Lee *et al*.

1984; Schieber 2010), and kerogen structures, which cannot be imaged using SEM owing to the small de Broglie wavelength of electrons (Williams and Carter 1996). Also, intergranular pores between clay minerals and pores associated with organic matter can be observed (Wu and Aguilera 2012; Ma *et al*. 2015). TEM has a limited field of view, and can only image small sample areas; because of this it tends to be combined with SEM for shale imaging (Chalmers *et al*. 2012; Bernard *et al*. 2013a).

X-ray radiography

X-ray radiography uses radiation energy to penetrate solid objects in order to assess variations in compositions; it produces 2D attenuation projections (Bouma 1978). It is used in the geosciences to image fossils and lithotype layers (Sopp 1900; Bottone 1906). In sedimentology, X- ray radiography can be used to image fabrics in shales and other sedimentary rocks at the core scale (Nuhfer *et al*. 1979; Algeo *et al*. 1994). X- ray radiography is a rapid 2D characterization tool and can provide information on the distribution of laminations, fractures and minerals, with increasingly extened application in 3D X-ray computed tomography (more details in section '3D X-ray computed tomography'(Algeo *et al*. 1994; O'Brien 1996; Cavé *et al*. 2009).

3D imaging techniques

3D X-ray computed tomography (XCT)

XCT is a widely used and versatile tool that can be applied to solve many problems of image based characterization in shales. It is particularly important in the study of shale as they are highly anisotropic and therefore any 2D image will not capture the full complexity of the rocks microstructure. This technique was first developed as a diagnositc medical technique by Godfrey Hounsfield (Hounsfield 1973) and Allan Cormack (Cormack 1980). The application of XCT to geoscience has been recognised since the 1980s (Wellington and Vinegar 1987), and is now widely used. For example in microstructure imaging, it can be used to quantify abundances of pores, minerals, and organic matter; XCT can also quantify the spatial connectivity and distribution of geological components (Sakellariou *et al*. 2003; Long *et al*. 2009; Curtis *et al*. 2012).

X-ray tomography images are generated based on the principle that X-ray intensity is linearly attenuated when passing through different materials (Hsieh 2009). Decrease in X-ray intensity is a function of X-ray energy, path length, and material linear attenuation coefficient (Wellington and Vinegar 1987; Dyson 1990). The sample rotates (typically 180°/360°) around a specific axis, and the detector measures the degree of attenuation creating 2D radiographs (projections) in grey-scale (Figure 3). Individual 2D radiograph images are reconstructed to produce a 3D volume (Wellington and Vinegar 1987; Ketcham and Carlson 2001; Hsieh 2009; Long *et al*. 2009).

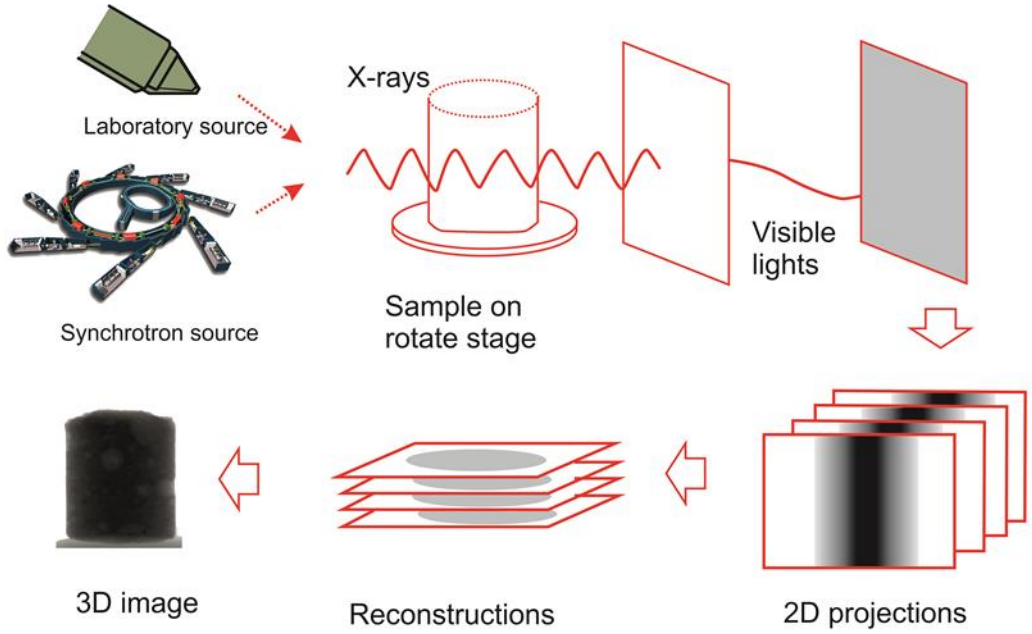

Figure 3 Schematic illustration of X-ray computed tomographical images acquisition and reconstruction, modified after (Landis and Keane 2010) .

The spatial resolution for cone beam systems normally used in laboratory XCT is determined by the focal spot size of the X-ray source. The geometric enlargement in X-ray microtomography (Micro-CT) depends on the distances between source, sample and detector (Stock 1999). While in parallel beam systems (used in synchrotron XCT) the maximum achievable spatial resolution is usually limited by detector pixel size (Cloetens *et al*. 1999). The type and thickness of the scintillator screen, the size of the source and mechanical stability of the instrument can also influence geometric enlargement in both cone and parallel beam systems (Maire and Withers 2014). Use of synchrotron X-ray sources significantly reduces acquisition times and improves spatial and contrast resolutions. The speed and improvement in resolutions enables the visualization of rapid chemical or physical reactions in shales (see section on '4D synchrotron XCT').

X-ray generators and detectors in XCT and micro-CT generally have relatively small spot diameters (0.5 – 10 µm) (Stock 1999), enabling textures and large minerals (normally > 2 µm) to be imaged at mesoscale and microscale in 3D. Nanoscale features such as matrix microstructures, nano-pores and some clay minerals cannot be resolved at these scales. X-ray nanotomography (Nano-CT) uses lens-based systems (either Fresnel zone plates or glass capillary condensers) enabling higher spatial resolutions (Withers 2007), and it can attain 50 nm spatial resolution (Withers 2007; Landis and Keane 2010).

The main challenge of image analysis is to identify different phases which includes mineral grains, organic matter particles and pores. For XCT, the phase difference in grey scale is based on different mineral attenuations, which can be calculated from Beer's law (Wellington and Vinegar 1987). The

energy used depends on the mineralogical composition and its thickness, and this should be decided prior to image acquisition. Laboratory sourced X-ray energy used in shale studies ranges from 20-85 keV, which results in a wide spectrum of X-ray attenuation values for different mineral phases (Keller *et al*. 2011; Kanitpanyacharoen *et al*. 2012; Robinet *et al*. 2012).

Some shale constituents cannot be identified in XCT data, making mineral identification and quantification difficult. For example, calcite and quartz have very similar X-ray attenuation values, but pyrite and carbon (in organic matter) have distinct attenuation values enabling identification (Figure 4). Where issues of similar X-ray attenuation arise, phase contrast XCT can be applied in both Micro-CT and Nano-CT. Phase contrast XCT converts phase variations in X-rays emerging from the imaged object into intensity variations at the X-ray detector to produce a difference in refractive index (Cloetens *et al*. 1996; Cloetens *et al*. 1999; Burvall *et al*. 2011). An example from the Haynesville Shale of the same area imaged by absorption and phase contrast (both Nano-CT) is shown in Figure 5. In absorption scans organic matter is clearly visible (Figure 5 a-b), while in phase contrast clay minerals are resolved (Figure 5 c-d). When phase-contrast is used details smaller than the pixel size of the detector can be detected (Cloetens *et al*. 1996).

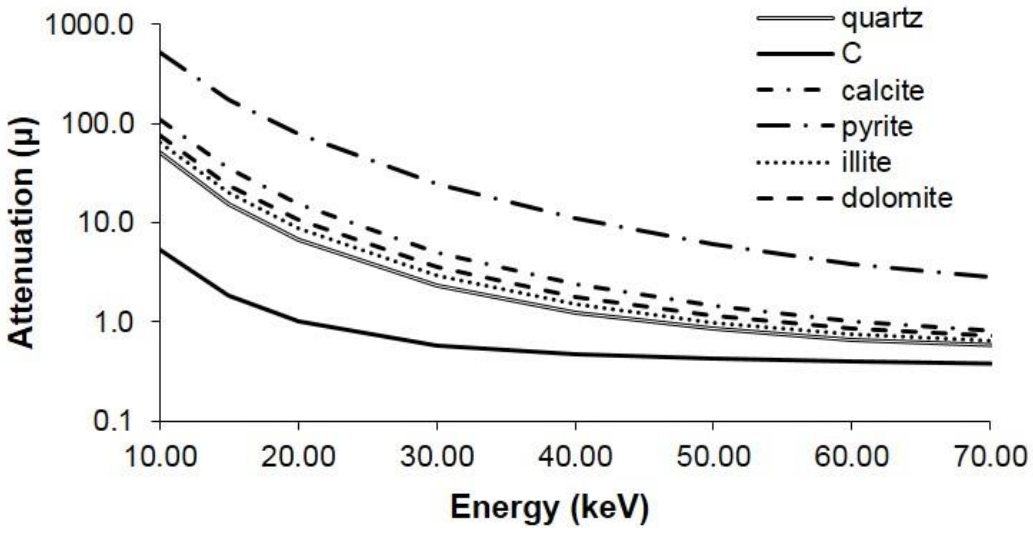

Figure 4 Varying mineral and element attenuation with increasing source energy, produced by MuCalcTool (http://www.ctlab.geo.utexas.edu/software/mucalctool/) .

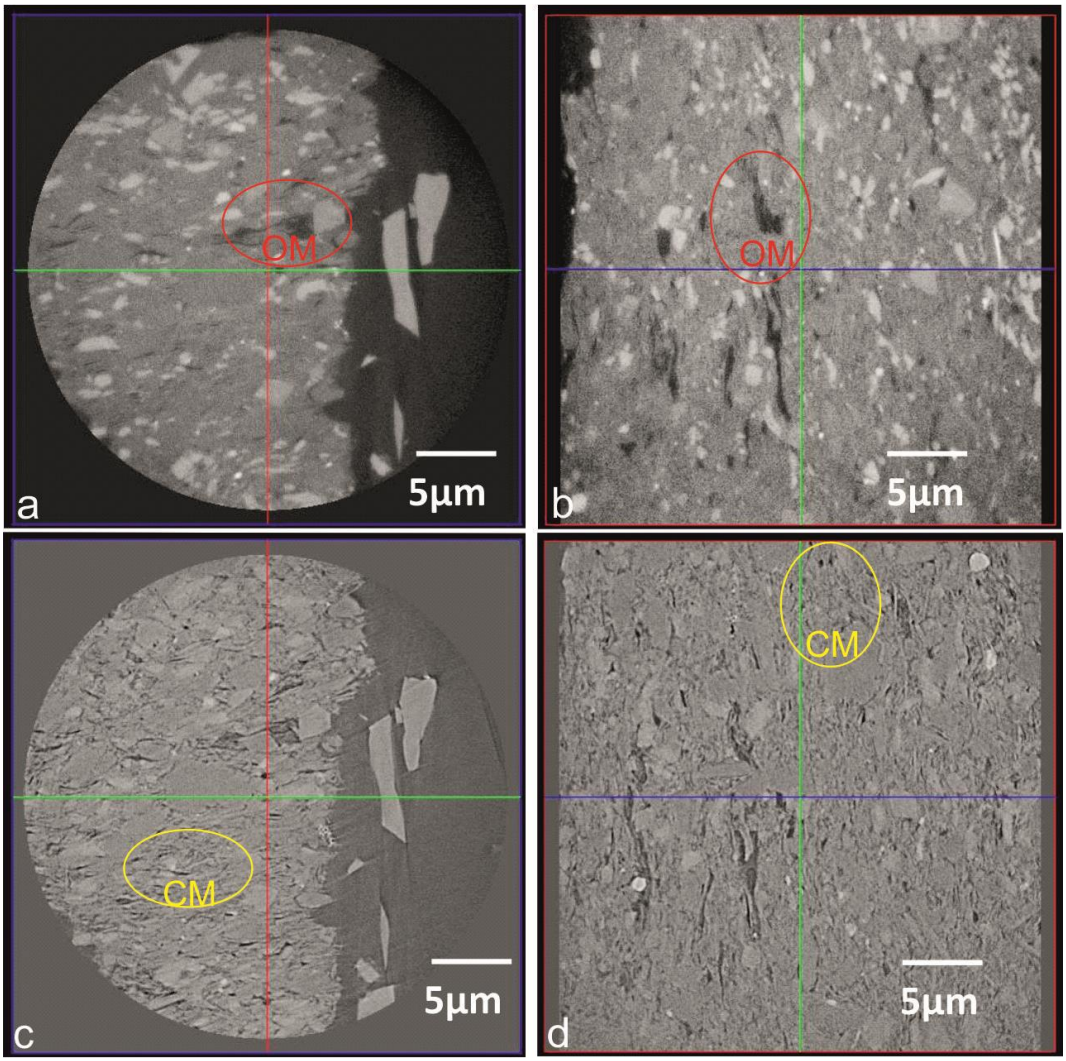

Figure 5 Same areas imaged by absorption scans and phase contrast scans in Nano-CT. A and B- absorption images, C and D- phase contrast images. OM- organic matter, CM-clay minerals

3D electron microscopy (3D-EM)

High-magnification 3D-EM can be used to image and characterise nanoscale features in shales including pores, fine-grained minerals and organic matter (Keller *et al*. 2013b; Hemes *et al*. 2015). Unlike XCT, 3D-EM is a destructive technique which can be described as continuous EM imaging during the systematic milling of thin layers of the sample surface (DeHoff 1983; Alkemper and Voorhees 2001). The sample layers can be removed either through physical slicing by an ultramicrotome as used in serial block face-scanning electron microscopy (SBF-SEM) or through ion milling systems such as focused ion beam scanning electron microscopy (FIB-SEM) (Figure 6).

Ultramicrotome serial block-face scanning electron microscopy (SBF-SEM):

SBF-SEM allows high-resolution imaging and highly-efficient image reconstructions (DeHoff 1983; Alkemper and Voorhees 2001). The system typically comprises an ultramicrotome coupled with a SEM detector (Rouquette *et al*. 2009) (Figure 6). The earliest generation of these systems produced

stereological image datasets through manual serial block-face methods, while later developments in automatic slicing and enhanced efficiency in image acquisition resulted in a reduced data collection time from weeks to hours (Alkemper and Voorhees 2001). The growth in computer based 3D image analysis has also enabled the combination of series of 2D slices in to 3D volumes (DeHoff 1983). The SBF-SEM technique produces high-resolution three dimensional images of shale microstructure, all be it in relatively small volumes (tens of microns) (Alkemper and Voorhees 2001; Ma 2016).

Focused Ion Beam Scanning Electron Microscopy (FIB-SEM):

The significance of the FIB-SEM techniques applied to shale samples has been noticed by many scholars, and has become one of the main techniques in nano-scale characterisation of pores (Sok *et al*. 2010; Curtis *et al*. 2012; Bernard *et al*. 2013b; Keller *et al*. 2013b). Recent studies using these techniques have characterised the type, size, geometric and topologic parameters of both pores and organic matter (Bernard *et al*. 2013b; Chen *et al*. 2013). Further studies have explored the relationship between pores, organic matter and minerals (Milliken *et al*. 2013; Ma *et al*. 2015).

The FIB milling technique uses a Ga^+ ion beam to produce an extremely flat surface (less than 20nm side damage); prior to this, Pt was deposited on the surface to protect the sample from curtaining (Curtis *et al*. 2010). Normal experimental setup involves the collection of hundreds of high-magnification SEM images (pixel size ~5 nm) collected at 5-20 nm intervals (Figure 6). It is a destructive technique. This allows fine-scale pores (<10 nm) to be observed and quantified (Curtis *et al*. 2010; Zhang *et al*. 2012; Keller *et al*. 2013b; Gaboreau *et al*. 2016). Due to the high magnification of images, there are severe limitations in sample size leading to issues around how representative datasets are. Therefore this technique should always be combined with larger scale techniques such as XCT or 2D SEM to confirm that the data collected is representative of heterogeneous shales (Houben *et al*. 2014; Hemes *et al*. 2015).7

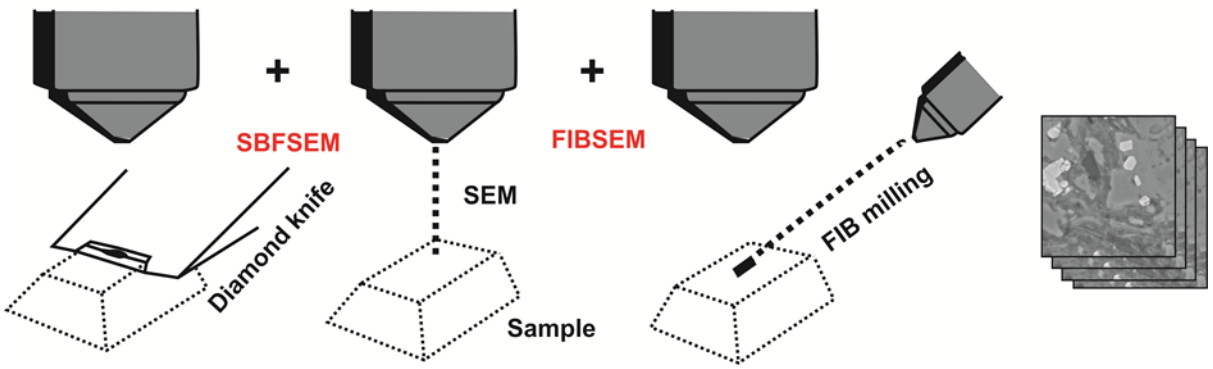

Figure 6 Schematic diagram of SBF-SEM and FIB-SEM, modified after (Arkill et al. 2014).

Complementary techniques in shale characterisation

Minerals

Shale mineral characterization can be undertaken using X-ray powder diffraction (XRD), electron backscatter diffraction (EBSD) and energy dispersive X-ray (EDX) techniques (Figure 1). Quantitative XRD is primarily used for phase identification of crystalline minerals in shale studies using powders (Mandile and Hutton 1995). EBSD can be used to identify minerals through the characterisation of crystal structure (Prior *et al*. 1999; Parsons *et al*. 2015). EDX analysis can also be used to provide elemental identification and quantitative compositional information alongside SEM imaging. Elemental mapping provides the 2D distribution of elements from which the mineral distribution can be derived (Ohkouchi *et al*. 2003; Curtis *et al*. 2010).

Organic matter

Aside from the volume and size of organic matter particles acquired through imaging methods, other organic matter properties such as organic matter concentration, chemical composition and thermal maturity are required to fully understand the roles of organic matter in shales. Commonly techniques include pyrolysis to obtain total organic carbon (TOC), EDX, pyrolysis–gas chromatography–mass spectrometry (GC/MS), Fourier transform infrared spectroscopy (FTIR) and fluorescence microscopy to obtain the chemical composition of shale components, and vitrinite reflectance (R_o) measurements to define maturity level (Figure 1).

TOC values are acquired after rock acidification and organic matter combustion (Byers *et al*. 1978), and this can be recalculated to a volume percentage allowing verification with organic matter volumes calculated from image quantification (Ma *et al*. 2016). Single spot EDX analysis of thin sections or stub mounted samples can provide confirmation of carbon present in organic matter particles EDX maps can also be used to map the distribution of organic matter in 2D and this works particularly well with SE- and BSE-SEM modes (Sondergeld *et al*. 2010a). Thermal measurements including R_o and T_{max} provide information on kerogen maturity to understand oil and gas generation and preservation processes (Bernard and Horsfield 2014; Romero-Sarmiento *et al*. 2014).

Pores

Combined with imaging methods, several other techniques can be utilised to measure both porosity and the size distribution of pores in shales. These include fluid penetration methods such as mercury intrusion porosimetry (MIP) (Klaver *et al*. 2012), helium pycnometry (Chalmers *et al*. 2012), physical adsorption methods utilising nitrogen and carbon dioxide (Clarkson *et al*. 2013), and small-angle scattering (SAS) techniques such as small angle X-ray scattering (SAXS) and small angle neutrons scattering (SANS) (Radlinski *et al*. 2004; Clarkson *et al*. 2013) (Figure 1).

Among fluid penetration and physical adsorption methods, MIP used in shale studies is limited because pore sizes below 3.5 nm cannot be measured, and these are often assumed to contribute a significant proportion of the total pores (Heath *et al*. 2011a; Kuila and Prasad 2013). Nitrogen adsorption has recently been widely used for pore size distribution measurements in shales as it can quantify fine pores in the 1.7 – 300 nm range, this is thought to encompass the majority of pores in shales (Kuila *et al*. 2012; Clarkson *et al*. 2013; Tian *et al*. 2013). SAS techniques allow a wide range of pore sizes to be measured from approximately 1-20,000 nm diameter by probing fluctuations in electronic density in SAXS or nuclear scattering cross section in SANS (Radlinski *et al*. 2004). Among these measurements, helium porosimetry, MIP and gas adsorption can only give the volume of connected pores. Helium porosimetry measures the largest range of pores, from nanoscale to microscale. Scattering methods can provide sizes of open and close pores but only with information on the sample surface. Imaging methods can measure both the volume and surface area of open and closed pores but they should normally be combined with complimentary techniques due to the low area/volume that imaging typically measures (Figure 1).

Application of multi-scale and multi-modal imaging of shale microstructure

Shale microstructure

Bedding/laminae

OM, X-ray radiography and XCT can provide information on macro- to meso-scale bedding/lamination in both 2D and 3D. With this information, an understanding of depositional processes, sequence stratigraphy and the properties controlling reservoir efficacy is possible.

Fabric in shales can be observed under OM (Loucks and Ruppel 2007). Laminations are dark and light coloured. The light laminations consist primarily of siliceous/carbonate minerals while the dark laminations consist of a greater proportion of clay minerals and heavy minerals (Figure 7 a). In the Tournemire Shale (France), clay mineral-rich lamination (illite, interstratified illite/smectite, chlorite, biotite) and non-clay grains laminations (carbonate, quartz, pyrite) in carbonate alternate (Charpentier *et al*. 2001).

Core-scale XCT imaging of the Sunbury Shale (US) (Figure 7 b) shows dark laminae containing more organic matter than the light laminae. Other features such as fractures and sulphide modules can also be observed (Algeo *et al*. 1994).

XCT can be used to spatially visualize laminations over a similar range to x-ray radiography (Coshell *et al*. 1994; Josh *et al*. 2012). 3D volume renderings show that laminations occur sub-parallel to the axis of the sample. Image slices perpendicular to bedding shows clear dark silty laminations and light pyrite (Josh *et al*. 2012) (Figure 7 c-d).

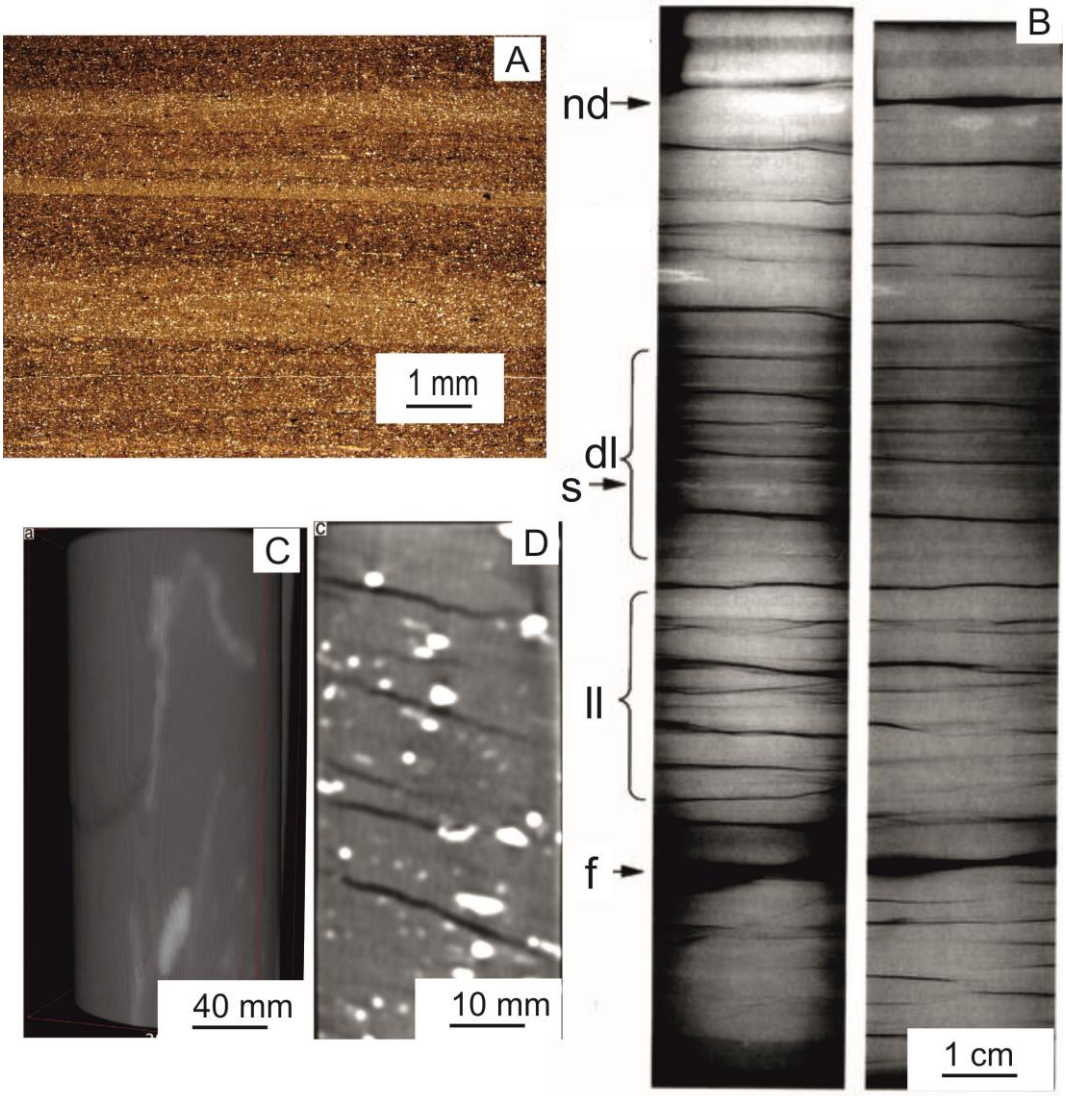

Figure 7. Images on bedding/laminae using OM, X-ray radiography and XCT. (a): optical microscope image (PPL) of laminate in shales in Lublin basin; (b) X-ray radiography of the laminated microstructure of Sunbury Shale (Algeo et al. 1994), dark laminae (d), light laminae (l), fractures (f) and sulphide modules (nd); (c & d): XCT images of sub-parallel laminations, (c) Volume rendering of laminae, (d)- 2D slice through 3D volume renderings, dark areas are silty laminations, bright areas are pyrite (Josh et al. 2012) .

Fractures

Fractures can be imaged using OM/SEM (Gale *et al*. 2014; Gasparrini *et al*. 2014) and XCT in 2D and 3D respectively (Kobchenko *et al*. 2011; Vega *et al*. 2014; Carey *et al*. 2015) (Figure 8 a-b). SEM (Chalmers *et al*. 2012; Wu and Aguilera 2012; Vega *et al*. 2014) and 3D-EM (Torsaeter *et al*. 2012; Chen *et al*. 2015) are commonly used for micro-scale imaging of fractures. Where fractures are cement-filled, combining optical microscopy with SEM imaging can provide mineralogical and microstrucutre information.

Some scholars (Vega *et al*. 2014; Ma 2016) have demonstrated the connectivities and heterogeneity of fractures and their distribution with minerals by using XCT (Figure 8 c). Recently, XCT is used for fracture characterisation because the sample can be imaged internally and also because image processing techniques enables the quantification and spatial distribution of shale components. Fractures (Figure 8 d) can also be imaged at the mesoscale (Kobchenko *et al*. 2011) and micro-scale (Barnettc Shale; Vega *et al*. 2014).

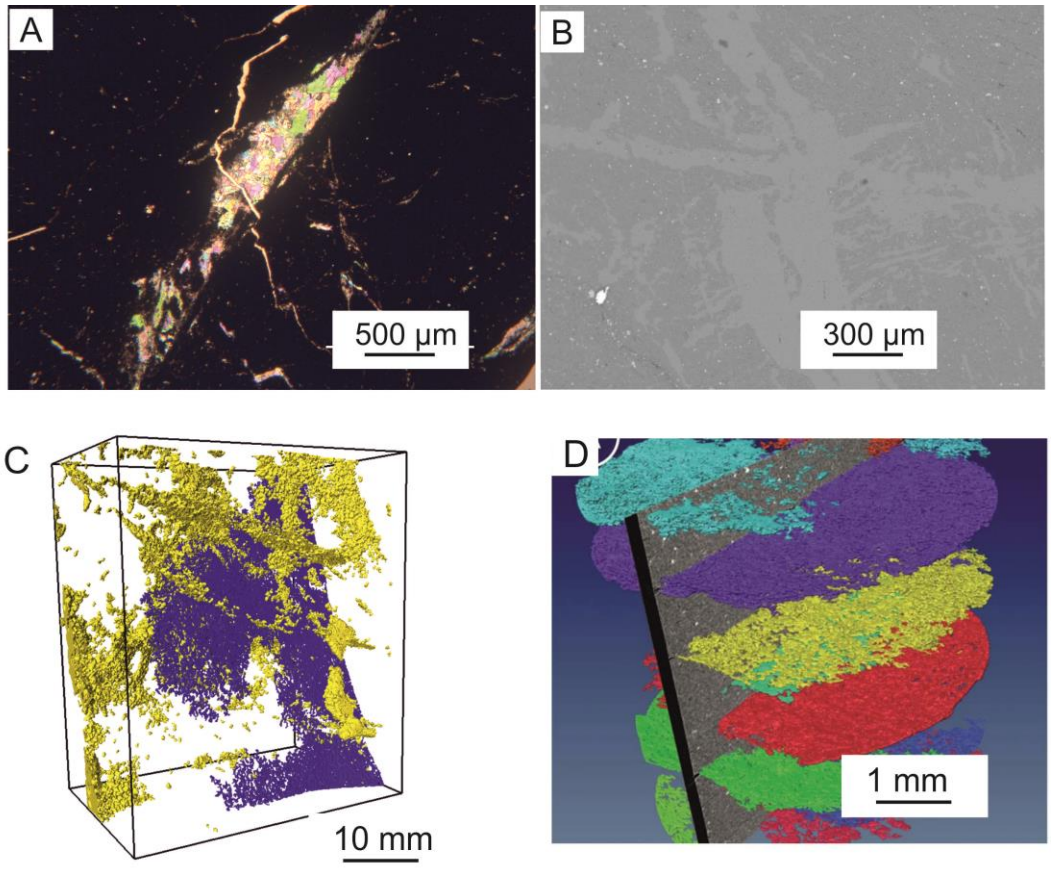

Figure 8. Fracture images from SEM and XCT techniques. (a) optical microscopy image (XPL) of calcite-filled fracture in shales in Lublin basin, Poland; (b) SEM image of calcite-filled fracture in shales in Lublin basin, Poland; (C): laboratory XCT image of calcite filled fractures (yellow) and open fractures (blue); (d) synchrotron sourced XCT image of meso-scale fractures in Green River Shale after heating (Kobchenko et al. 2011).

Minerals and organic matter

Minerals and organic matter vary from meso- to nano-scale in size, and they can be imaged using a range of techniques including OM, SEM, TEM, XCT and 3D-EM. Using OM and SEM (Krinsley *et al*. 1983; Prior *et al*. 1999) petrologic characteristics of mineral components can be described. From these descriptions, interpretations about the deposition environment and diagenetic development of the shale can be made (Kim *et al*. 1998; Milliken *et al*. 2012; Taylor and Macquaker 2014). Organic matter particles can also be observed using OM and SEM, especially in organic-rich samples (Figure 9 a) (Milner et al. 2010b; Curtis et al. 2011a). Nanoscale features such as the texture of clay minerals can be imaged using TEM in shale samples (Figure 9 b) (Largeau *et al*. 1990; Bernard *et al*. 2012) .

Using X-ray microtomography and nanotomography (Kanitpanyacharoen *et al*. 2012; Zhang *et al*. 2012; Vega *et al*. 2014), silt-size minerals and silt-size organic matter can be imaged in 3D. Three phases including pyrites, minerals, and micropores (and fractures and kerogen) in Posidonia Shale (Figure 9 c) were quantified using x-ray microtomography (Kanitpanyacharoen *et al*. 2012). Minerals, matrix and organic matter were selected for pore model in a Devonian shale sample using X-ray nanotomography (Zhang *et al*. 2012).

Some shale components cannot be clearly imaged using XCT because they are smaller than the spatial resolution of the technique or lower than the contrast resolution; this is a particular problem when more than one small component is mixed. For example, clay minerals and granular minerals mixed in one phase and kerogen and pores mixed in another phase (Figure 9 d) in Barnett Shale (Vega *et al*. 2014). 3D-EM would be required to image these regions (Curtis *et al*. 2010; Zhang *et al*. 2012; Ma *et al*. 2016). Clay minerals, organic matter and pores can be identified and segmented in 3D using SBF-SEM (Figure 9 e-f) (Ma *et al*. 2016). The geometry, orientation, thickness and connectivity of isolated shale components can then be quantified. FIB-SEM is also commonly used in shale studies. For example, a Barnett Shale study (Curtis *et al*. 2010) has reported that the inorganic matrix contains dispersed kerogen, within which variable numbers of pores were observed (Figure 9 g-h).

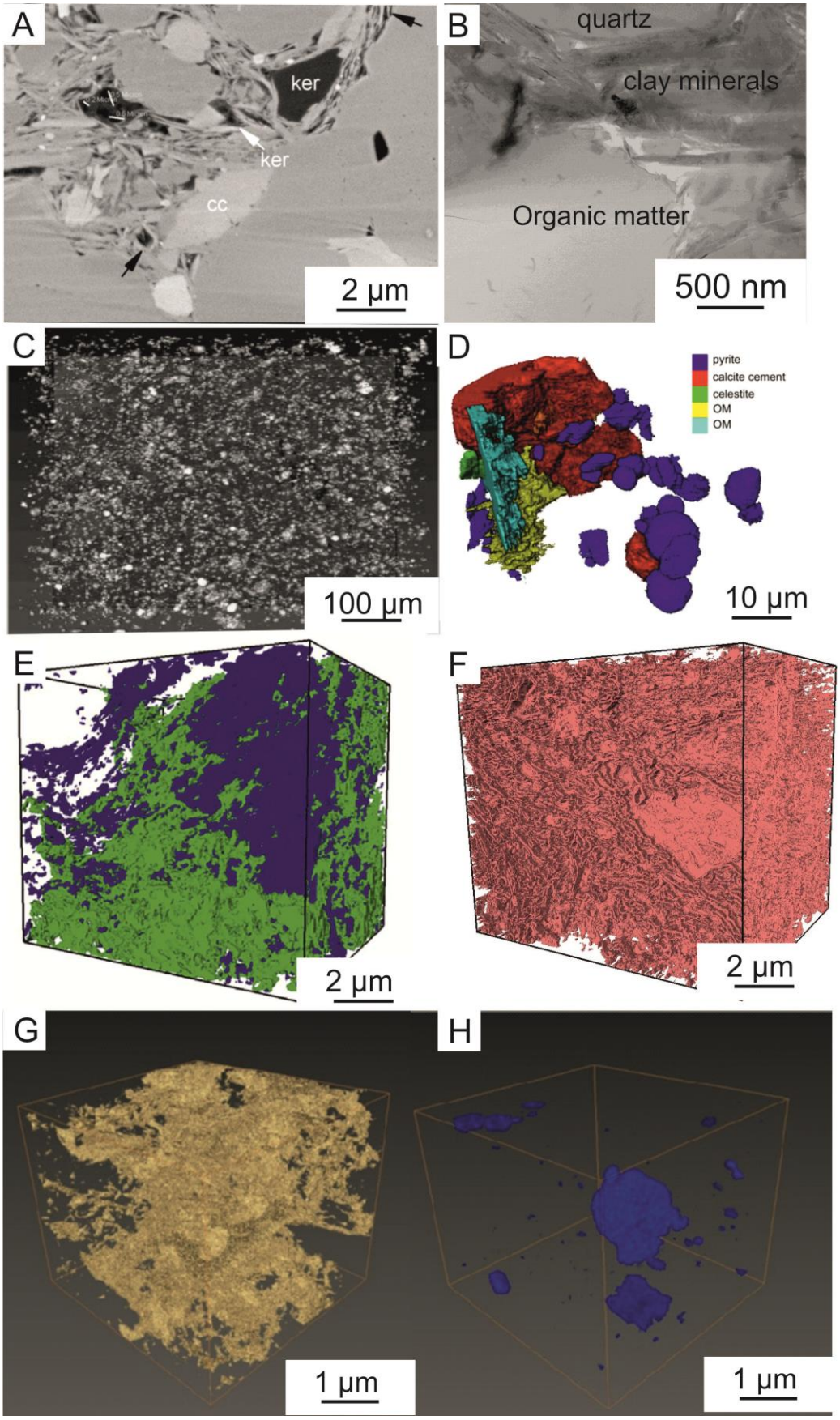

Figure 9 Mineral and organic matter imaged using 2D and 3D techniques. (a) BSE image of mineral grains and kerogen in the Hayneville Shale (Milner et al. 2010a); (b) TEM image of organic matter, clay

minerals and quartz in a Haynesville shale sample; (c) synchrotron sourced X-ray microtomography image of pyrite in Posidonia Shale (Kanitpanyacharoen et al. 2012); (d) laboratory sourced X-ray nanotomography image of minerals and organic matter in the Barnett Shale (blue- pyrite, red –calcite cements, green- celestite, yellow and light blue –organic matter) (Vega et al. 2014); (e-f) SBF-SEM images of organic matter (green- connected organic matter, blue- isolated organic matter) and clay minerals (pink) in the Bowland Shale (Ma et al. 2016); (g-h) FIB-SEM images of organic matter (yellow) and pyrite (blue), modified after Curtis (et al., 2012)

Pores

SEM and TEM can provide 2D images for pore type identification (Figure 10 a-c), while 3D XCT and 3D-EM can provide spatial information. An example of the imaging of three pore types is in the Bowland Shale (Figure 10 d-f), in this study the morphological features of pores were quantified and contrasted in 3D (Ma *et al*. 2016).

In gas shale systems worldwide (Curtis *et al*. 2010; Milliken *et al*. 2013; Sondergeld *et al*. 2013), organic matter pores which occur inside or around organic matter particles range in size from macropores to nanopores, and often have ellipsoidal or spherical shapes (Milliken *et al*. 2013). Inter-mineral pores occur between mineral grains, crystals and clay mineral platelets.(Loucks *et al*. 2012; Jiao *et al*. 2014). Some inter-mineral mesopores can only be observed using TEM (Bernard *et al*. 2013a), particularly where pores occur between clay platelets (Schieber 2010) (Figure 9 b). Intra-mineral pores are commonly found within pyrite framboids, or within fossil bodies (Loucks *et al*. 2012; Klaver *et al*. 2015).

Based on 2D and 3D images, further studies of pores can be perfomed. Some studies in several shale plays have reported a relationship between increasing thermal maturity and organic matter porosity generation (Curtis *et al*. 2011a; Sondergeld *et al*. 2013; Curtis *et al*. 2014). Data from 3D-EM imaging can also be used to build pore network models from which gas storage and transport studies can be developed (Keller *et al*. 2011; Dewers *et al*. 2012; Peng *et al*. 2015). Ambrose *et al*. (2010) used imaging datasets to build kerogen and pore networks from which gas-in-place volumes were calculated. Quantification of the 3D geometry and topology of pore pathways can be built on basis of segmented pore, and gas transport could be analysed from the development of pore network models (Keller *et al*. 2011; Zou *et al*. 2015)(Figure 10 g-h)

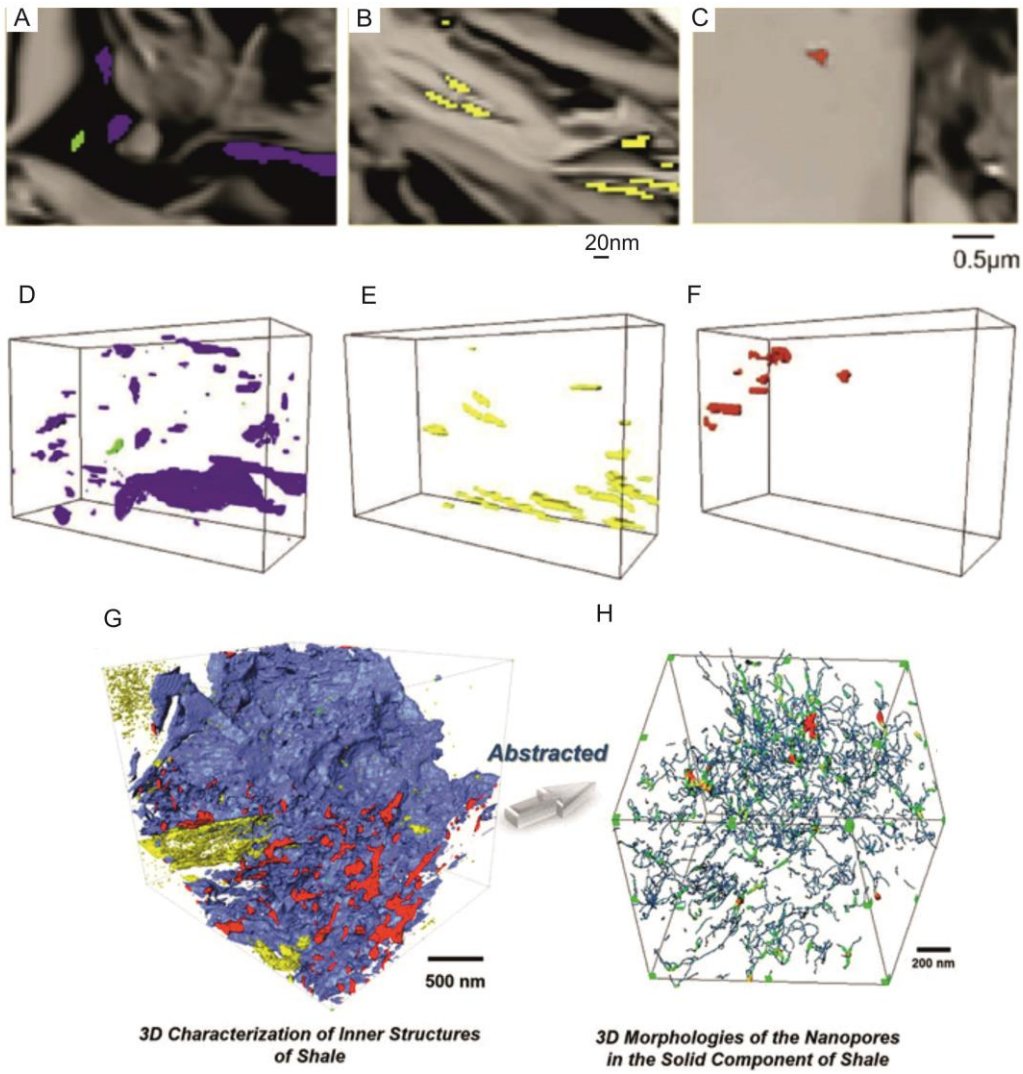

Figure 10 2D and 3D pore images and reconstructed pore networks. (a) SEM image of macropores and mesopores associated with organic matter, green- pores inside organic matter, purple- pores at the interface of organic matter and minerals (b) SEM image of pores between clay mineral grains; (c) SEM image of mesopores inside minerals; (d-f) SBF-SEM images of Bowland Shale pore types, (d) organic matter-associated pores, (e) interparticle pores, and (f) intraparticle pores (Ma et al. 2016); (g) Nano-CT and FIB-SEM images of pores and other structure in shales, blue- rock matrix, yellow- high-density mineral, red- pores; (h) pore network extracted from (g) (Zou et al. 2015).

Image quantification

Quantitative microstructural characterization

Prior to the separation of minerals and other phases in shale image datasets, a series of image processing steps are required. The processes outlined below are based on grey-scale images acquired by XCT images and 2D/3D EM images. In XCT datasets, following the collection of a series of 2D images by the X-ray detector, the 2D images must be 'reconstructed' to produce a 3D data volume.

The reconstruction processes typically uses the common centre of rotation of all the 2D images and a computer algorithm to combine all the 2D images in to a 3D volume (Mersereau and Oppenheim 1974; Dudgeon and Mersereau 1984). Similarly in 3D EM datasets there are often slight misalignments between each slice, and the 2D image stack must be aligned to build a 3D volume. Filtering of the 3D volumes in both XCT and EM is also required. Filtering reduces noise in the dataset and can make different phases or the interface between phases more visible. There are many different filtering algorithms (Nagao and Matsuyama 1979; Yoo 2004; Russ 2011). Median filter, non-local means filter and edge-preserving smoothing filter are three common filters used for shale images (Kanitpanyacharoen *et al*. 2013; Ma *et al*. 2016). Segmentation is the process that separates the 3D image into discrete components. Segmentation is typically done on the basis of the grey scale values for individual pixels (Yoo 2004; Russ 2011). On the basis of its grey scale value each pixel in the 3D volume is plotted on a histogram. A particular phase is segmented based on a range grey scale values within the histogram. The value range is based on the shape, size, distribution and relative grey scale values of particular volumes within the 3D data (Yoo 2004; Korfiatis *et al*. 2007; Stauber and Müller 2008; Landis and Keane 2010; Russ 2011). 2D image processing incorporates filtering and segmentation.

Once a 2D image dataset has been segmented the characteristics of the shale components can quantified. Attributes of individual and groups of components including size, area, elongation index, orientation, convexity, circularity (Robinet *et al*., 2012; Fauchille *et al*., 2014, Klaver *et al*., 2015) can be measured, calculated and mapped. For 3D datasets, more quantitative spatial and inter-relational information can be collected. The full 3D morphology of individual shale components can be measured, and further calculations based on these measurements can be made (equivalent diameter, volume, surface area, geometry, orientation etc.). The advantage with 3D datasets over 2D datasets in shales is that the connectivity and distribution of networks of shale components can be quantified (Pierret *et al*. 2002; Loucks *et al*. 2009; Ross and Bustin 2009; Russ 2011; Keller *et al*. 2013a; Ma 2016).

2D and 3D time-sequence images acquired with either EM or XCT can be quantitatively compared through optical imaging techniques such as Digital Image Correlation (DIC) or Digital Volume Correlation (DVC), respectively (Bay *et al*., 1999;Wang *et al*., 2013-2014; Figueroa Pilz *et al*.). DIC and DVC enable the quantification of displacements, strains and crack apertures at the surface and within samples (Allais, 1994; Bay *et al*., 1999; Bornert *et al*., 2010; Mostafavi *et al*., 2015; Valle *et al*., 2015). The application in shales (Desrues and Viggiani, 2004, Lenoir *et al*., 2007; Hedan *et al*., 2012-2014, Fauchille *et al*., 2016) includes the thermo, hydraulic or mechanical behaviour (eg. strains, crack location, crack generation, crack apertures, kerogen transformation, gas adsorption and flow).

598 ***Representative analysis***

599 In multi-scale studies of shales, how features of interest are identified and quantified is important. Of
600 particular importance is the prediction and modelling of petrophysical properties including
601 permeability, diffusion, deformation and electrical conductivity (Mishra and Akbar 2011; Yoon and
602 Dewers 2013; Saraji and Piri 2015). The acquisition of representative data in very heterogeneous
603 materials is a fundamental problem in shale characterisation. Knowing how representative a sample
604 volume is in highly heterogeneous rocks is key to ensuring that data can be properly and accurately
605 applied Representative elementary area (REA) or representative elementary volume (REV)
606 calculations (Mishra and Akbar 2011) are one way to do this. These calculations are commonly
607 defined as: the minimum area or volume of the image set that is large enough to capture a
608 representative amount of the heterogeneity (Bear and Braester 1972; Gitman *et al*. 2007). REV is
609 normally calculated for one specific parameter in accurate conditions (e.g. scale, error criteria and
610 method) and could be different for another parameter on the same volume observed.
611 Different approaches exist to calculate REV of multi-scale imaging in natural materials. One method
612 that has been applied to shales is the 'counting box method' (Houben *et al*. 2014; Fauchille 2015; Ma
613 *et al*. 2016).
614 Within the entire measured volume, sub-volumes are incrementally increased from the centre or at
615 stochastic points chosen at random. Within each sub-volume, the volume fraction (or another chosen
616 parameter) of a specific phase is measured and then plotted with the side length of each volume. The
617 REV is determined as the minimum volume with an accepted oscillation with a maximum relative
618 error of 10% in comparison with the whole volume (Gitman *et al*. 2007; Al-Raoush and Papadopoulos
619 2010). It is worth noting that the REV of some particular parameters such as particle size distribution,
620 coordination number or physical parameters might not be the same with the volume percentages of
621 particles (Al-Raoush and Papadopoulos 2010).
622 In some sandstone and carbonate reservoirs, REV can be 5–20 times the median particle size (Vik *et*
623 *al*. 2013). In shale samples, REVs side for porosity can range from 5-10 µm with image resolutions
624 10-80 nm (Yoon and Dewers 2013; Ma *et al*. 2016) to 25 µm with image resolutions ~100 nm (Gelb
625 *et al*. 2011). REV for intra-organic pores have been reported as less than 1 µm (Chen *et al*. 2013).
626 REA side for organic matter and minerals in Posidonia Shale is calculated to be approximately 140
627 µm for. Other methods quantifying the fluctuations of a specific parameter are also used in shale, for
628 example, homogeneization areas based on Hifler theory of percolation (Keller *et al*. 2013b; Cosenza
629 *et al*. 2015b).
630
631

Challenges and Future Perspectives

Advanced imaging techniques

4D Synchrotron XCT

In the last decade, synchrotron based time-resolved XCT (4D) has become a standard tool in many engineering fields for the analysis of *in situ* deformation of materials (Cai *et al*., 2014; Karagadde *et al*., 2015; Mostafavi *et al*., 2015). The application of synchrotron 4D XCT to the study of shale is in its early stages, but it can be used for very rapid imaging and qualitative study of thermal maturation (Kobchenko *et al*. 2011) and natural or induced fracture development.

Pore and fluid generation in kerogen has been observed with increasing temperature, enabling models of kerogen maturity (Kobchenko *et al*. 2011) and primary hydrocarbon migration (Panahi *et al*. 2014) to be built. During thermal maturation experiments (Kobchenko *et al*. 2011; Tiwari *et al*. 2013), temperature effects on shale were detected from 300-500°C, and strain localization was visible after X-ray image registration.

The application of time-resolved image modelling has the potential to unravel complex morphological interaction between the microstructure of shale and the anisotropic mechanical responses during mechanical loading (Cai *et al*. 2016).

Neutron imaging

Neutron imaging is also a powerful, non-destructive method enabling the internal structure of a material to be quantified (Perfect *et al*. 2014). However, one of the fundamental differences between neutron imaging and X-ray imaging is the feasibility of obtaining images from different materials. Using neutron imaging, it is normally easier to image light elements (with low atomic number) than X-ray techniques, including (amongst many others) carbon, water, and hydrogen. In addition, the neutrons can also penetrate the high spectra of elements with higher atomic numbers that for example include lead and titanium (IAEA 2008). In the context of shales, porosity is measured using neutron emission tools from either chemical or electronic sources (De Beer *et al*. 2004; Perfect *et al*. 2014) that interact with the molecules of the rocks and fluid during the wellbore completion.

Upscaling

Representative results at larger scales

Ultra-high resolution techniques and tools (Gelb *et al*. 2011) can improve the microstructure characterisation of shales; however, as resolution increases the field of view generally decreases. When planning shale imaging a balance should be made between the number of features of interest, the image resolution and the size of the area or volume of the image (which indirectly defines the scale of analysis). This ensures that a significant REV value for the dataset will be calculated.

Gigapixel SEM image mosaics are increasingly used in shales (Klaver *et al*. 2012; Robinet *et al*. 2012; Fauchille 2015) and heterogeneous materials (Prêt *et al*. 2010b; Vergès and Morales 2014). The acquisition of gigapixel images allows high resolution 2D areas at the micrometre to millimetre scale to be imaged and enables a multi-scale approach on the same sample. This can reduce erroneous data interpretation on small areas. SEM imaging at different scales is also possible through defocusing the electron beam at various resolutions. Pore structure can also be characterized by TEM image mosaics; however, sample sizes for TEM imaging are very limited, in contrast to centimetre-sized samples for SEM. XCT and 3D-EM image volume mosaics can also be employed, but this is challenging in XCT because of large image overlaps (around 50%) in cylinder-shaped scans and long acquisition times especially in strongly heterogeneous shales.

Upscaling to log- or basin-scale

The aim of upscaling data to log- or basin-scale is to understand and model the petrophysical properties at various scales. It can enable accurate in-place resources to be calculated and calculate potential produced volumes in shale reservoirs. Ideally, microstructure image analysis should be performed on samples from different depths in the basin and for different shale facies, so variability microstructure and petrophysical properties can be quantified. There is potential for upscaled, high resolution microstructure and petrophysical properties from different depths and facies to be directly linked to well log or seismic data sets for accurate reservoir prediction (Ma 2016).

Image based modelling

Flow simulation

Due to the low permeability of shale ($<10^{-18}$ m^2), understanding oil and gas fluid flow remains a challenge, and this requires long-term petrophysical measurements to quantify shale response over long periods (Mckernan *et al*. 2014). To describe the behaviour of shale in a more efficient way, image modelling techniques have been proposed.

Studies of flow simulation using data from 2D and 3D imaging techniques (Peng *et al*. 2015; Archilha *et al*. 2016), is still limited because of issues with image resolution and representative scales. For example, pores below 10nm that are normally unresolvable using the XCT or SEM imaging, can be measured by other techniques such as nitrogen adsorption and SANS and incorporated into multi-scale 3D models (Tariq *et al*. 2011; Ma *et al*. 2016). These very small pores (nm scale) may form a locally connected flow path for gas molecules (Javadpour *et al*. 2007). Nanometre scale pores can be built into whole pore models when combined with larger pores (>10nm) in imaging data.

Fracture simulation

Unlocking natural gas and oil trapped in shale formations is an increasingly important challenge in the oil and gas industry. Hydraulic fracturing combined with horizontal drilling facilitates the extraction

of oil and gas (Arthur *et al*. 2008; Rahm 2011). Image based modelling could be a powerful tool in the simulation of mechanical behaviour during hydraulic fracturing in shale. As discussed in 2.2, information from imaging datasets on microstructure, mineralogical composition, component morphology, porosity, and permeability may be important in understanding how shales respond mechanically during fracturing. The challenge is to model and predict fracture development in shales based on multi-scale image datasets. From models, accurate description and quantification of the mechanical response of shales during loading conditions should be possible. This work will have applications in petroleum, civil, mining and nuclear operations.

Acknowledgements

The authors would like to acknowledge the support of the Manchester X-ray Imaging Facility (MXIF), the Electron Microscopy Centre at the University of Manchester, the Diamond Manchester Collaboration, and the Research Complex at Harwell. Aspects of the work presented here have been partly supported by funds from EPSRC (EP/I02249X/1), NERC (NE/M007286/1), the Chinese Scholarship Council, Chevron, BG Group and Schlumberger; all of which is gratefully acknowledged.

References

Agar, S.M., Prior, D.J. & Behrmann, J.H. 1989. Back-scattered electron imagery of the tectonic fabrics of some fine-grained sediments: implications for fabric nomenclature and deformation processes. *Geology*, **17**, 901-904.

Al-Raoush, R. & Papadopoulos, A. 2010. Representative elementary volume analysis of porous media using X-ray computed tomography. *Powder technology*, **200**, 69-77.

Algeo, T.J., Phillips, M., Jaminski, J. & Fenwick, M. 1994. High-Resolution X-Radiography of Laminated Sediment Cores: RESEARCH METHOD PAPER. *Journal of Sedimentary Research*, **64**.

Alkemper, J. & Voorhees, P. 2001. Quantitative serial sectioning analysis. *Journal of Microscopy*, **201**, 388-394.

Ambrose, R.J., Hartman, R.C., Diaz-Campos, M., Akkutlu, Y. & Sondergeld, C.H. 2010. New Pore-scale Considerations for Shale Gas in Place Calculations. *Petroleum Engineers Unconventional Gas Conference*. Society of Petroleum Engineers, Pittsburgh, Pennsylvania.

Aplin, A.C., Matenaar, I.F., McCarty, D.K. & van Der Pluijm, B.A. 2006. Influence of mechanical compaction and clay mineral diagenesis on the microfabric and pore-scale properties of deep-water Gulf of Mexico mudstones. *Clays and Clay Minerals*, **54**, 500-514.

Archilha, N., Missagia, R., Hollis, C., de Ceia, M., McDonald, S., Lima Neto, I., Eastwood, D. & Lee, P. 2016. Permeability and acoustic velocity controlling factors determined from X-ray tomography images of carbonate rocks. *AAPG Bulletin*.

Arkill, K.P., Qvortrup, K., Starborg, T., Mantell, J.M., Knupp, C., Michel, C.C., Harper, S.J., Salmon, A.H., Squire, J.M. & Bates, D.O. 2014. Resolution of the three dimensional structure of components of the glomerular filtration barrier. *BMC Nephrology*, **15**, 1.

737 Arthur, J.D., Bohm, B. & Layne, M. 2008. Hydraulic fracturing considerations for natural gas wells of
738 the Marcellus Shale. *Groundwater Protection Council Annual Forum. Cincinnati*.

739 Bear, J. & Braester, C. 1972. On the Flow of Two Immscible Fluids in Fractured Porous Media.
740 *Developments in Soil Science*, **2**, 177-202.

741 Bernard, S., Brown, L., Wirth, R., Schreiber, A., Schulz, H.-M., Horsfield, B., Aplin, A.C. & Mathia,
742 E.J. 2013a. FIB-SEM and TEM investigations of an organic-rich shale maturation series from the
743 lower Toarcian Posidonia Shale, Germany: Nanoscale pore system and fluid-rock interactions.
744 *Electron microscopy of shale hydrocarbon reservoirs: AAPG Memoir*, **102**, 53-66.

745 Bernard, S., Brown, L., Wirth, R., Schreiber, A., Schulz, H.-M., Horsfield, B., Aplin, A.C. & Mathia,
746 E.J. 2013b. FIB-SEM and TEM Investigations of an Organic-rich Shale Maturation Series from the
747 Lower Toarcian Posidonia Shale, Germany: Nanoscale Pore System and Fluid-rock Interactions.
748 *Electron Microscopy of Shale Hydrocarbon Reservoirs: AAPG Memoir 102*, **102**, 53.

749 Bernard, S. & Horsfield, B. 2014. Thermal maturation of gas shale systems. *Annual Review of Earth*
750 *and Planetary Sciences*, **42**, 635-651.

751 Bernard, S., Wirth, R., Schreiber, A., Schulz, H.-M. & Horsfield, B. 2012. Formation of nanoporous
752 pyrobitumen residues during maturation of the Barnett Shale (Fort Worth Basin). *International*
753 *Journal of Coal Geology*, **103**, 3-11.

754 Bin, B., Rukai, Z., Songtao, W., Wenjing, Y., Gelb, J., Gu, A., ZHANG, X. & Ling, S. 2013. Multi-
755 scale method of Nano (Micro)-CT study on microscopic pore structure of tight sandstone of
756 Yanchang Formation, Ordos Basin. *Petroleum Exploration and Development*, **40**, 354-358.

757 Bobko, C. & Ulm, F.-J. 2008. The nano-mechanical morphology of shale. *Mechanics of Materials*, **40**,
758 318-337.

759 Bonnelye, A., Schubnel, A., David, C., Henry, P., Guglielmi, Y., Gout, C., Fauchille, A.L. & Dick, P.
760 2016a. Elastic wave velocity evolution of shales deformed under uppermost-crustal conditions.
761 *Journal of Geophysical Research: Solid Earth*.

762 Bonnelye, A., Schubnel, A., David, C., Henry, P., Guglielmi, Y., Gout, C., Fauchille, A.L. & Dick, P.
763 2016b. Strength anisotropy of shales deformed under uppermost-crustal conditions. *Journal of*
764 *Geophysical Research: Solid Earth*.

765 Bossart, P. & Thury, M. 2007. Research in the Mont Terri Rock laboratory: quo vadis? *Physics and*
766 *Chemistry of the Earth, Parts A/B/C*, **32**, 19-31.

767 Bottone, S.R. 1906. Radiography and the'X'rays in practice and theory: with constructional and
768 manipulatory details. New York.

769 Bouma, A.H. 1978. X-ray radiography. *Sedimentology*. Springer, 1279-1280.

770 Buchardt, B. & Lewan, M. 1990. Reflectance of vitrinite-like macerals as a thermal maturity index for
771 Cambrian-Ordovician Alum shale, southern Scandinavia (1). *AAPG Bulletin*, **74**, 394-406.

772 Burvall, A., Lundström, U., Takman, P.A., Larsson, D.H. & Hertz, H.M. 2011. Phase retrieval in X-
773 ray phase-contrast imaging suitable for tomography. *Optics express*, **19**, 10359-10376.

774 Bustin, Bustin, Cui, Ross & Pathi, M. 2008. Impact of Shale Properties on Pore Structure and Storage
775 Characteristics. *In*: Engineers, S.o.P. (ed.) *SPE Shale Gas Production Conference*, . Society of
776 Petroleum Engineers Fort Worth, Texas, USA.

777 Byers, S.C., Mills, E.L. & Stewart, P.L. 1978. A comparison of methods of determining organic
778 carbon in marine sediments, with suggestions for a standard method. *Hydrobiologia*, **58**, 43-47.

779 Cai, B., Lee, P.D., Karagadde, S., Marrow, T.J. & Connolley, T. 2016. Time-resolved synchrotron
780 tomographic quantification of deformation during indentation of an equiaxed semi-solid granular
781 alloy. *Acta Materialia*, **105**, 338-346, doi: http://dx.doi.org/10.1016/j.actamat.2015.11.028.

Carey, J.W., Lei, Z., Rougier, E., Mori, H. & Viswanathan, H. 2015. Fracture-permeability behavior of shale. *Journal of Unconventional Oil and Gas Resources*, **11**, 27-43, doi: http://dx.doi.org/10.1016/j.juogr.2015.04.003.

Cariou, S., Dormieux, L. & Skoczylas, F. 2013. An original constitutive law for Callovo-Oxfordian argillite, a two-scale double-porosity material. *Applied Clay Science*, **80**, 18-30.

Cavé, L., Al, T., Xiang, Y. & Vilks, P. 2009. A technique for estimating one-dimensional diffusion coefficients in low-permeability sedimentary rock using X-ray radiography: Comparison with through-diffusion measurements. *Journal of contaminant hydrology*, **103**, 1-12.

Chadwick, R., Zweigel, P., Gregersen, U., Kirby, G., Holloway, S. & Johannessen, P. 2004. Geological reservoir characterization of a CO 2 storage site: the Utsira Sand, Sleipner, northern North Sea. *Energy*, **29**, 1371-1381.

Chalmers, G.R., Bustin, R.M. & Power, I.M. 2012. Characterization of gas shale pore systems by porosimetry, pycnometry, surface area, and field emission scanning electron microscopy/transmission electron microscopy image analyses: Examples from the Barnett, Woodford, Haynesville, Marcellus, and Doig units. *AAPG Bulletin*, **96**, 1099-1119.

Charpentier, D., Cathelineau, M., Mosser-Ruck, R. & Bruno, G. 2001. Mineralogical evolution of argilites in dehydrated-oxidised zones: the example of the argilitic walls from Tournemire tunnel.

Chen, C., Hu, D., Westacott, D. & Loveless, D. 2013. Nanometer-scale characterization of microscopic pores in shale kerogen by image analysis and pore-scale modeling. *Geochemistry, Geophysics, Geosystems*, **14**, 4066-4075.

Chen, L., Zhang, L., Kang, Q., Viswanathan, H.S., Yao, J. & Tao, W. 2015. Nanoscale simulation of shale transport properties using the lattice Boltzmann method: permeability and diffusivity. *Scientific reports*, **5**.

Chiou, W., Faas, R., Kasprowicz, J., Li, H., Lomenick, T., OBrien, N., Pamukcu, S., Smart, P., Weaver, C. & Yamamoto, T. 2012. Microstructure of fine-grained sediments: From Mud to Shale. Springer Science & Business Media.

Clarkson, Jensen & Chipperfield. 2012. Unconventional gas reservoir evaluation: What do we have to consider? *Journal of Natural Gas Science and Engineering*, 9-33.

Clarkson, C.R., Solano, N., Bustin, R.M., Bustin, A.M.M., Chalmers, G.R.L., He, L., Melnichenko, Y.B., Radliński, A.P. & Blach, T.P. 2013. Pore structure characterization of North American shale gas reservoirs using USANS/SANS, gas adsorption, and mercury intrusion. *Fuel*, **103**, 606-616.

Cloetens, P., Barrett, R., Baruchel, J., Guigay, J.-P. & Schlenker, M. 1996. Phase objects in synchrotron radiation hard x-ray imaging. *Journal of Physics D: Applied Physics*, **29**, 133.

Cloetens, P., Ludwig, W., Baruchel, J., Guigay, J.-P., Pernot-Rejmánková, P., Salomé-Pateyron, M., Schlenker, M., Buffière, J.-Y., Maire, E. & Peix, G. 1999. Hard x-ray phase imaging using simple propagation of a coherent synchrotron radiation beam. *Journal of Physics D: Applied Physics*, **32**, A145.

Conacher, H. 1917. VIII. A Study of Oil Shales and Torbanites. *Transactions of the Geological Society of Glasgow*, **16**, 164-192.

Cormack, A.M. 1980. Recollections of my work with computer assisted tomography. *Molecular and cellular biochemistry*, **32**, 57-61.

Cosenza, P., Prêt, D., Giraud, A. & Hedan, S. 2015a. Effect of the local clay distribution on the effective elastic properties of shales. *Mechanics of Materials*, **84**, 55-74.

Cosenza, P., Pret, D. & Zamora, M. 2015b. Effect of the local clay distribution on the effective electrical conductivity of clay rocks. *Journal of Geophysical Research: Solid Earth*, **120**, 145-168.

827 Coshell, L., McLver, R.G. & Chang, R. 1994. X-ray computed tomography of Australian oil shales:
828 non-destructive visualization and density determination. *Fuel*, **73**, 1317-1321, doi:
829 http://dx.doi.org/10.1016/0016-2361(94)90307-7.

830 Curtis, J.B. 2002. Fractured shale-gas systems. *AAPG Bulletin*, **86**, 1921-1938.

831 Curtis, M.E., Ambrose, R.J. & Sondergeld, C.H. 2010. Structural Characterization of Gas Shales on
832 the Micro- and Nano-Scales. *Canadian Unconventional Resources and International Petroleum*
833 *Conference*. Society of Petroleum Engineers.

834 Curtis, M.E., Ambrose, R.J., Sondergeld, C.H. & Rai, C.S. 2011a. Investigation of the relationship
835 between organic porosity and thermal maturity in the Marcellus Shale. *North American*
836 *Unconventional Gas Conference and Exhibition*. Society of Petroleum Engineers.

837 Curtis, M.E., Ambrose, R.J., Sondergeld, C.H. & Rai, C.S. 2011b. Transmission and Scanning
838 Electron Microscopy Investigation of Pore Connectivity of Gas Shales on the Nanoscale. *North*
839 *American Unconventional Gas Conference and Exhibition*. Society of Petroleum Engineers.

840 Curtis, M.E., Goergen, E., Jernigen, J., Sondergeld, C.H. & Rai, C.S. 2014. High-Resolution Mapping
841 of the Distribution and Connectivity of Organic Matter in Shales. *SPE Annual Technical Conference*
842 *and Exhibition*. Society of Petroleum Engineers.

843 Curtis, M.E., Sondergeld, C.H., Ambrose, R.J. & Rai, C.S. 2012. Microstructural investigation of gas
844 shales in two and three dimensions using nanometer-scale resolution imaging. *AAPG Bulletin*, **96**,
845 665-677.

846 Day-Stirrat, R.J., Aplin, A.C., Środoń, J. & Van der Pluijm, B.A. 2008. Diagenetic reorientation of
847 phyllosilicate minerals in Paleogene mudstones of the Podhale Basin, southern Poland. *Clays and*
848 *Clay Minerals*, **56**, 100-111.

849 Day-Stirrat, R.J., Dutton, S.P., Milliken, K.L., Loucks, R.G., Aplin, A.C., Hillier, S. & van der Pluijm,
850 B.A. 2010. Fabric anisotropy induced by primary depositional variations in the silt: clay ratio in two
851 fine-grained slope fan complexes: Texas Gulf Coast and northern North Sea. *Sedimentary Geology*,
852 **226**, 42-53, doi: http://dx.doi.org/10.1016/j.sedgeo.2010.02.007.

853 De Beer, F.C., Middleton, M.F. & Hilson, J. 2004. Neutron radiography of porous rocks and iron ore.
854 *Applied Radiation and Isotopes*, **61**, 487-495.

855 DeHoff, R. 1983. Quantitative serial sectioning analysis: preview. *Journal of Microscopy*, **131**, 259-
856 263.

857 Dewers, T.A., Heath, J., Ewy, R. & Duranti, L. 2012. Three-dimensional pore networks and transport
858 properties of a shale gas formation determined from focused ion beam serial imaging. *International*
859 *Journal of Oil, Gas and Coal Technology*, **5**, 229-248.

860 Donovan, J.J., Pingitore, N.E. & Westphal, A. 2003. Compositional averaging of backscatter
861 intensities in compounds. *Microscopy and Microanalysis*, **9**, 202-215.

862 Dudgeon, D.E. & Mersereau, R.M. 1984. Multidimensional digital signal processing. *Prentice-Hall*
863 *Signal Processing Series, Englewood Cliffs: Prentice-Hall, 1984*, **1**.

864 Dyson, N.A. 1990. X-rays in Atomic and Nuclear Physics. Cambridge University Press.

865 EIA, U. 2015. *Annual Energy Outlook 2015*.

866 Etminan, S.R., Javadpour, F., Maini, B.B. & Chen, Z. 2014. Measurement of gas storage processes in
867 shale and of the molecular diffusion coefficient in kerogen. *International Journal of Coal Geology*,
868 **123**, 10-19, doi: http://dx.doi.org/10.1016/j.coal.2013.10.007.

869 Fauchille, A., Hedan, S., Prêt, D., Valle, V., Cabrera, J. & Cosenza, P. 2014. Relationships between
870 desiccation cracking behavior and microstructure of the Tournemire clay rock by coupling DIC and
871 SEM methods. *Proceedings of IS on Geomechanics from Micro to Macro, Cambridge, lUK*, 1421-
872 1424.

873 Fauchille, A.L. 2015. *Determinismes microstructuraux et mineralogiques de la fissuration hydrique*
874 *dans les argilites de Tournemire : apports couples de la petrographie quantitative et de la correlation*
875 *d'images numeriques*. PhD, University of Poitiers, France.

876 Fauchille, A.L., Hédan, S., Prêt, D., Valle, V., Cabrera, J. & Cosenza, P. 2016. Multi-scale study of
877 the deformation and the cracking of a clay-rock sample. *Applied Clay Sciences*.

878 Foscolos, A., Powell, T. & Gunther, P. 1976. The use of clay minerals and inorganic and organic
879 geochemical indicators for evaluating the degree of diagenesis and oil generating potential of shales.
880 *Geochimica Et Cosmochimica Acta*, **40**, 953-966.

881 Gaboreau, S., Prêt, D., Tinseau, E., Claret, F., Pellegrini, D. & Stammose, D. 2011. 15 years of in situ
882 cement–argillite interaction from Tournemire URL: Characterisation of the multi-scale spatial
883 heterogeneities of pore space evolution. *Applied Geochemistry*, **26**, 2159-2171.

884 Gaboreau, S., Robinet, J.-C. & Prêt, D. 2016. Optimization of pore-network characterization of a
885 compacted clay material by TEM and FIB/SEM imaging. *Microporous and Mesoporous Materials*,
886 **224**, 116-128.

887 Gale, J.F., Laubach, S.E., Olson, J.E., Eichhubl, P. & Fall, A. 2014. Natural fractures in shale: A
888 review and new observations. *AAPG Bulletin*, **98**, 2165-2216.

889 Gasparik, M., Bertier, P., Gensterblum, Y., Ghanizadeh, A., Krooss, B.M. & Littke, R. 2014.
890 Geological controls on the methane storage capacity in organic-rich shales. *International Journal of*
891 *Coal Geology*, **123**, 34-51, doi: http://dx.doi.org/10.1016/j.coal.2013.06.010.

892 Gasparrini, M., Sassi, W. & Gale, J.F.W. 2014. Natural sealed fractures in mudrocks: A case study
893 tied to burial history from the Barnett Shale, Fort Worth Basin, Texas, USA. *Marine and Petroleum*
894 *Geology*, **55**, 122-141, doi: http://dx.doi.org/10.1016/j.marpetgeo.2013.12.006.

895 Gelb, J., Gu, A., Fong, T., Hunter, L., Lau, S. & Yun, W. 2011. A closer look at shale: Representative
896 elementary volume analysis with laboratory 3D X-Ray computed microtomography and
897 nanotomography. *Proc. SCA*.

898 Gipson Jr, M. 1965. Application of the electron microscope to the study of particle orientation and
899 fissility in shale. *Journal of Sedimentary Research*, **35**.

900 Giraud, A., Huynh, Q.V., Hoxha, D. & Kondo, D. 2007. Effective poroelastic properties of
901 transversely isotropic rock-like composites with arbitrarily oriented ellipsoidal inclusions. *Mechanics*
902 *of Materials*, **39**, 1006-1024.

903 Gitman, I.M., Askes, H. & Sluys, L.J. 2007. Representative volume: Existence and size determination.
904 *Engineering Fracture Mechanics*, **74**, 2518-2534, doi:
905 http://dx.doi.org/10.1016/j.engfracmech.2006.12.021.

906 Heath, J.E., Dewers, T.A., McPherson, B.J., Petrusak, R., Chidsey, T.C., Rinehart, A.J. & Mozley,
907 P.S. 2011a. Pore networks in continental and marine mudstones: Characteristics and controls on
908 sealing behavior. *Geosphere*, **7**, 429-454.

909 Heath, J.E., Dewers, T.A., McPherson, B.J.O.L., Petrusak, R., Chidsey, T.C., Rinehart, A.J. & Mozley,
910 P.S. 2011b. Pore networks in continental and marine mudstones: Characteristics and controls on
911 sealing behavior. *Geosphere*, **7**, 429-454, doi: 10.1130/GES00619.1.

912 Hedan, S., Cosenza, P., Valle, V., Dudoignon, P., Fauchille, A.-L. & Cabrera, J. 2012. Investigation
913 of the damage induced by desiccation and heating of Tournemire argillite using digital image
914 correlation. *International Journal of Rock Mechanics and Mining Sciences*, **51**, 64-75, doi:
915 http://dx.doi.org/10.1016/j.ijrmms.2012.01.001.

916 Hedan, S., Fauchille, A.-L., Valle, V., Cabrera, J. & Cosenza, P. 2014. One-year monitoring of
917 desiccation cracks in Tournemire argillite using digital image correlation. *International Journal of*
918 *Rock Mechanics and Mining Sciences*, **68**, 22-35, doi: http://dx.doi.org/10.1016/j.ijrmms.2014.02.006.

Hemes, S., Desbois, G., Urai, J.L., Schröppel, B. & Schwarz, J.-O. 2015. Multi-scale characterization of porosity in Boom Clay (HADES-level, Mol, Belgium) using a combination of X-ray μ-CT, 2D BIB-SEM and FIB-SEM tomography. *Microporous and Mesoporous Materials*, **208**, 1-20.

Hornby, B.E. 1998. Experimental laboratory determination of the dynamic elastic properties of wet, drained shales. *Journal of Geophysical Research: Solid Earth*, **103**, 29945-29964.

Horseman, S., Higgo, J., Alexander, J. & Harrington, J. 1996. Water, gas and solute movement through argillaceous media. *Nuclear Energy Agency Rep. CC-96/1. OECD, Paris*.

Houben, M., Desbois, G., Urai, J., de Winter, D., Drury, M. & Schwarz, J. 2014. Microstructure of the shaly facies of opalinus clay on the Mm-nm scale. *Fourth EAGE Shale Workshop*.

Hounsfield, G.N. 1973. Computerized transverse axial scanning (tomography): Part 1. Description of system. *British Journal of Radiology*, **46**, 1016-1022.

Hsieh, J. 2009. Computed tomography: principles, design, artifacts, and recent advances. SPIE, Bellingham.

IAEA. 2008. *The IAEA Database of Natural Matrix Reference Materials*.

IUPAC. 1994. Physical Chemistry Division Commission on Colloid and Surface Chemistry, Subcommittee on Characterization of Porous Solids: Recommendations for the characterization of porous solids (Technical Report). *Pure and Applied Chemistry*, **66** 1739-1758.

Jarvie, D.M., Hill, R.J., Ruble, T.E. & Pollastro, R.M. 2007. Unconventional shale-gas systems: The Mississippian Barnett Shale of north-central Texas as one model for thermogenic shale-gas assessment. *AAPG Bulletin*, **91**, 475-499.

Javadpour, F. 2009. Nanopores and Apparent Permeability of Gas Flow in Mudrocks (Shales and Siltstone). *Journal of Canadian Petroleum Technology*, **Volume 48,**, 16-21, doi: 10.2118/09-08-16-DA.

Javadpour, F., Fisher, D. & Unsworth, M. 2007. Nanoscale gas flow in shale gas Sediments. *Journal of Canadian Petroleum Technology*, **46**, 55-61.

Jiao, K., Yao, S., Liu, C., Gao, Y., Wu, H., Li, M. & Tang, Z. 2014. The characterization and quantitative analysis of nanopores in unconventional gas reservoirs utilizing FESEM–FIB and image processing: An example from the lower Silurian Longmaxi Shale, upper Yangtze region, China. *International Journal of Coal Geology*, **128–129**, 1-11, doi: http://dx.doi.org/10.1016/j.coal.2014.03.004.

Jorand, R. 2006. *Etude expérimentale de la conductivité thermique: application au forage EST 205 du site de Meuse/Haute Marne (ANDRA)*, Institut de Physique du Globe de Paris.

Josh, M., Esteban, L., Delle Piane, C., Sarout, J., Dewhurst, D.N. & Clennell, M.B. 2012. Laboratory characterisation of shale properties. *Journal of Petroleum Science and Engineering*, **88–89**, 107-124, doi: 10.1016/j.petrol.2012.01.023.

Kaarsberg, E.A. 1959. Introductory studies of natural and artificial argillaceous aggregates by sound-propagation and X-ray diffraction methods. *The Journal of Geology*, 447-472.

Kanitpanyacharoen, W., Kets, F.B., Wenk, H.-R. & Wirth, R. 2012. Mineral preferred orientation and microstructure in the Posidonia shale in relation to different degrees of thermal maturity. *Clays and Clay Minerals*, **60**, 315-329.

Kanitpanyacharoen, W., Parkinson, D.Y., De Carlo, F., Marone, F., Stampanoni, M., Mokso, R., MacDowell, A. & Wenk, H.-R. 2013. A comparative study of X-ray tomographic microscopy on shales at different synchrotron facilities: ALS, APS and SLS. *Journal of synchrotron radiation*, **20**, 172-180.

Keller, L.M., Holzer, L., Schuetz, P. & Gasser, P. 2013a. Pore space relevant for gas permeability in Opalinus clay: Statistical analysis of homogeneity, percolation, and representative volume element. *Journal of Geophysical Research: Solid Earth*, **118**, 2799-2812.

966 Keller, L.M., Holzer, L., Wepf, R. & Gasser, P. 2011. 3D geometry and topology of pore pathways in
967 Opalinus clay: Implications for mass transport. *Applied Clay Science*, **52**, 85-95, doi:
968 http://dx.doi.org/10.1016/j.clay.2011.02.003.

969 Keller, L.M., Schuetz, P., Erni, R., Rossell, M.D., Lucas, F., Gasser, P. & Holzer, L. 2013b.
970 Characterization of multi-scale microstructural features in Opalinus Clay. *Microporous and*
971 *Mesoporous Materials*, **170**, 83-94, doi: http://dx.doi.org/10.1016/j.micromeso.2012.11.029.

972 Ketcham, R.A. & Carlson, W.D. 2001. Acquisition, optimization and interpretation of X-ray
973 computed tomographic imagery: applications to the geosciences. *Computers & Geosciences*, **27**,
974 381-400, doi: 10.1016/s0098-3004(00)00116-3.

975 Kim, J.-W., Bryant, W., Watkins, J. & Tieh, T. 1998. Electron microscopic observations of shale
976 diagenesis, offshore Louisiana, USA, Gulf of Mexico. *Geo-Marine Letters*, **18**, 234-240.

977 Klaver, J., Desbois, G., Littke, R. & Urai, J.L. 2015. BIB-SEM characterization of pore space
978 morphology and distribution in postmature to overmature samples from the Haynesville and Bossier
979 Shales. *Marine and Petroleum Geology*, **59**, 451-466, doi:
980 http://dx.doi.org/10.1016/j.marpetgeo.2014.09.020.

981 Klaver, J., Desbois, G., Urai, J.L. & Littke, R. 2012. BIB-SEM study of the pore space morphology in
982 early mature Posidonia Shale from the Hils area, Germany. *International Journal of Coal Geology*,
983 **103**, 12-25, doi: http://dx.doi.org/10.1016/j.coal.2012.06.012.

984 Knudsen, M. 1934. The Kinetic Theory of Gases, Methuen & Co. *Ltd., London*.

985 Kobchenko, M., Panahi, H., Renard, F., Dysthe, D.K., Malthe-Sørenssen, A., Mazzini, A., Scheibert,
986 J., Jamtveit, B. & Meakin, P. 2011. 4D imaging of fracturing in organic-rich shales during heating. *J.*
987 *Geophys. Res.*, **116**, B12201, doi: 10.1029/2011jb008565.

988 Korfiatis, P., Skiadopoulos, S., Sakellaropoulos, P., Kalogeropoulou, C. & Costaridou, L. 2007.
989 Combining 2D wavelet edge highlighting and 3D thresholding for lung segmentation in thin-slice CT.
990 *British Journal of Radiology*, **80**, 996-1004.

991 Krinsley, D., Pye, K. & Kearsley, A. 1983. Application of backscattered electron microscopy in shale
992 petrology. *Geological Magazine*, **120**, 109-114.

993 Krinsley, D.H., Pye, K., Boggs Jr, S. & Tovey, N.K. 2005. Backscattered scanning electron
994 microscopy and image analysis of sediments and sedimentary rocks. Cambridge University Press.

995 Kuila, U. & Prasad, M. 2013. Specific surface area and pore-size distribution in clays and shales.
996 *Geophysical Prospecting*, **61**, 341-362.

997 Kuila, U., Prasad, M., Derkowski, A. & McCarty, D.K. 2012. Compositional Controls on Mudrock
998 Pore-Size Distribution: An Example from Niobrara Formation. *SPE Annual Technical Conference*
999 *and Exhibition*. Society of Petroleum Engineers, San Antonio, Texas, USA.

1000 Kumar, V., Sondergeld, C.H. & Rai, C.S. 2012. Nano to Macro Mechanical Characterization of Shale.
1001 *SPE Annual Technical Conference and Exhibition*. Society of Petroleum Engineers, San Antonio,
1002 Texas, USA.

1003 Landis, E.N. & Keane, D.T. 2010. X-ray microtomography. *Materials Characterization*, **61**, 1305-
1004 1316, doi: http://dx.doi.org/10.1016/j.matchar.2010.09.012.

1005 Largeau, C., Derenne, S., Casadevall, E., Berkaloff, C., Corolleur, M., Lugardon, B., Raynaud, J. &
1006 Connan, J. 1990. Occurrence and origin of "ultralaminar" structures in "amorphous" kerogens of
1007 various source rocks and oil shales. *Organic Geochemistry*, **16**, 889-895.

1008 Lazar, O.R., Bohacs, K.M., Macquaker, J.H., Schieber, J. & Demko, T.M. 2015. Capturing key
1009 attributes of fine-grained sedimentary rocks in outcrops, cores, and thin sections: nomenclature and
1010 description guidelines. *Journal of Sedimentary Research*, **85**, 230-246.

1011 Lee, J.H., Peacor, D.R., Lewis, D.D. & Wintsch, R.P. 1984. Chlorite-illite/muscovite interlayered and
1012 interstratified crystals: a TEM/STEM study. *Contributions to Mineralogy and Petrology*, **88**, 372-385.

1013 Lemmens, H. & Butcher, A. 2011. A Workflow Concept To Characterize Core Samples From The
1014 Microscale To The Nanoscale. *SPE Annual Technical Conference and Exhibition*. Society of
1015 Petroleum Engineers, Denver, Colorado, USA.

1016 Long, H., Swennen, R., Foubert, A., Dierick, M. & Jacobs, P. 2009. 3D quantification of mineral
1017 components and porosity distribution in Westphalian C sandstone by microfocus X-ray computed
1018 tomography. *Sedimentary Geology*, **220**, 116-125, doi: http://dx.doi.org/10.1016/j.sedgeo.2009.07.003.

1019 Loucks, R.G., Reed, R.M., Ruppel, S.C. & Hammes, U. 2012. Spectrum of pore types and networks
1020 in mudrocks and a descriptive classification for matrix-related mudrock pores. *AAPG Bulletin*, **96**,
1021 1071-1098.

1022 Loucks, R.G., Reed, R.M., Ruppel, S.C. & Jarvie, D.M. 2009. Morphology, Genesis, and Distribution
1023 of Nanometer-Scale Pores in Siliceous Mudstones of the Mississippian Barnett Shale. *Journal of*
1024 *Sedimentary Research*, **79**, 848-861.

1025 Loucks, R.G. & Ruppel, S.C. 2007. Mississippian Barnett Shale: Lithofacies and depositional setting
1026 of a deep-water shale-gas succession in the Fort Worth Basin, Texas. *AAPG Bulletin*, **91**, 579-601.

1027 Ma, L. 2016. *Multi-scale 3D imaging of the microstructure in organic-rich shales.* PhD, University of
1028 Manchester.

1029 Ma, L., Taylor, K.G., Lee, P.D., Dobson, K.J., Dowey, P.J. & Courtois, L. 2016. Novel 3D
1030 centimetre-to nano-scale quantification of an organic-rich mudstone: The Carboniferous Bowland
1031 Shale, Northern England. *Marine and Petroleum Geology*, **72**, 193-205, doi:
1032 http://dx.doi.org/10.1016/j.marpetgeo.2016.02.008.

1033 Ma, Y., Zhong, N., Li, D., Pan, Z., Cheng, L. & Liu, K. 2015. Organic matter/clay mineral
1034 intergranular pores in the Lower Cambrian Lujiaping Shale in the north-eastern part of the upper
1035 Yangtze area, China: A possible microscopic mechanism for gas preservation. *International Journal*
1036 *of Coal Geology*, **137**, 38-54, doi: http://dx.doi.org/10.1016/j.coal.2014.11.001.

1037 Maire, E. & Withers, P. 2014. Quantitative X-ray tomography. *International Materials Reviews*, **59**,
1038 1-43.

1039 Mallants, D., Marivoet, J. & Sillen, X. 2001. Performance assessment of the disposal of vitrified high-
1040 level waste in a clay layer. *Journal of Nuclear Materials*, **298**, 125-135.

1041 Mandile, A.J. & Hutton, A.C. 1995. Quantitative X-ray diffraction analysis of mineral and organic
1042 phases in organic-rich rocks. *International Journal of Coal Geology*, **28**, 51-69.

1043 Mastalerz, M., He, L.L., Melnichenko, Y.B. & Rupp, J.A. 2012. Porosity of Coal and Shale: Insights
1044 from Gas Adsorption and SANS/USANS Techniques. *Energy & Fuels*, **26**, 5109-5120, doi: Doi
1045 10.1021/Ef300735t.

1046 Mckernan, R., Rutter, E., Mecklenburgh, J., Taylor, K. & Covey-Crump, S. 2014. Influence of
1047 Effective Pressure on Mudstone Matrix Permeability: Implications for Shale Gas Production.
1048 *SPE/EAGE European Unconventional Resources Conference and Exhibition*. Society of Petroleum
1049 Engineers.

1050 Mersereau, R.M. & Oppenheim, A.V. 1974. Digital reconstruction of multidimensional signals from
1051 their projections. *Proceedings of the IEEE*, **62**, 1319-1338.

1052 Milliken, K.L. & Curtis, M.E. 2016. Imaging pores in sedimentary rocks: Foundation of porosity
1053 prediction. *Marine and Petroleum Geology*, **73**, 590-608, doi:
1054 http://dx.doi.org/10.1016/j.marpetgeo.2016.03.020.

1055 Milliken, K.L. & Day-Stirrat, R.J. 2013. Cementation in mudrocks: brief review with examples from
1056 cratonic basin mudrocks.

1057 Milliken, K.L., Esch, W.L., Reed, R.M. & Zhang, T. 2012. Grain assemblages and strong diagenetic
1058 overprinting in siliceous mudrocks, Barnett Shale (Mississippian), Fort Worth Basin, Texas. *AAPG*
1059 *Bulletin*, **96**, 1553-1578.

Milliken, K.L., Rudnicki, M., Awwiller, D.N. & Zhang, T. 2013. Organic matter–hosted pore system, Marcellus Formation (Devonian), Pennsylvania. *AAPG Bulletin*, **97**, 177-200.

Milner, M., McLin, R. & Petriello, J. 2010a. Imaging Texture and Porosity in Mudstones and Shales: Comparison of Secondary and Ion-Milled Backscatter SEM Methods. Society of Petroleum Engineers.

Milner, M., McLin, R. & Petriello, J. 2010b. Imaging Texture and Porosity in Mudstones and Shales: Comparison of Secondary and Ion-Milled Backscatter SEM Methods. *Canadian Unconventional Resources and International Petroleum Conference*. Society of Petroleum Engineers, Calgary, Alberta, Canada.

Mishra, P.K. & Akbar, B. 2011. Effectiveness of Digital Rock Physical Laboratories In Characterisation Of Heterogenous And Complex Carbonates- A Synthesis. *International Petroleum Technology Conference*. International Petroleum Technology Conference, Bangkok, Thailand.

Nagao, M. & Matsuyama, T. 1979. Edge preserving smoothing. *Computer graphics and image processing*, **9**, 394-407.

Nix, T. & Feist-Burkhardt, S. 2003. New methods applied to the microstructure analysis of Messel oil shale: confocal laser scanning microscopy (CLSM) and environmental scanning electron microscopy (ESEM). *Geological Magazine*, **140**, 469-478.

Nuhfer, E.B., Vinopal, R.J. & Klanderman, D.S. 1979. *X-radiograph atlas of lithotypes and other structures in the Devonian shale sequence of West Virginia and Virginia.* West Virginia Geological and Economic Survey, Morgantown (USA).

O'Brien, N.R. 1996. Shale lamination and sedimentary processes. *Geological Society, London, Special Publications*, **116**, 23-36.

Ohkouchi, N., Kuroda, J.i., Okada, M. & Tokuyama, H. 2003. Why Cretaceous black shales have high C/N ratios: Implications from SEM-EDX observations for Livello Bonarelli black shales at the Cenomanian-Turonian boundary. *Earth Evol*, **1**, 239-241.

Ortega, Ulm & Abousleiman. 2010. A Multi-scale Micromechanics Framework For Shale Using Nano-tools. American Rock Mechanics Association.

Ortega, J.A., Ulm, F.-J. & Abousleiman, Y. 2007. The effect of the nanogranular nature of shale on their poroelastic behavior. *Acta Geotechnica*, **2**, 155-182.

Panahi, H., Kobchenko, M., Renard, F., Mazzini, A., Scheibert, J., Dysthe, D.K., Jamtveit, B., Malthe-Sørenssen, A. & Meakin, P. 2014. A 4D synchrotron X-ray tomography study of the formation of hydrocarbon migration pathways in heated organic-rich shale. *arXiv preprint arXiv:1401.2448*.

Parsons, I., Gerald, J.D.F. & Lee, M.R. 2015. Review. Routine characterization and interpretation of complex alkali feldspar intergrowths. *American Mineralogist*, **100**, 1277-1303.

Peng, S., Yang, J., Xiao, X., Loucks, B., Ruppel, S. & Zhang, T. 2015. An Integrated Method for Upscaling Pore-Network Characterization and Permeability Estimation: Example from the Mississippian Barnett Shale. *Transport in Porous Media*, 1-18, doi: 10.1007/s11242-015-0523-8.

Perfect, E., Cheng, C.L., Kang, M., Bilheux, H.Z., Lamanna, J.M., Gragg, M.J. & Wright, D.M. 2014. Neutron imaging of hydrogen-rich fluids in geomaterials and engineered porous media: A review. *Earth-Science Reviews*, **129**, 120-135, doi: http://dx.doi.org/10.1016/j.earscirev.2013.11.012.

Pham, Q., Vales, F., Malinsky, L., Minh, D.N. & Gharbi, H. 2007. Effects of desaturation–resaturation on mudstone. *Physics and Chemistry of the Earth, Parts A/B/C*, **32**, 646-655.

Pierret, A., Capowiez, Y., Belzunces, L. & Moran, C.J. 2002. 3D reconstruction and quantification of macropores using X-ray computed tomography and image analysis. *Geoderma*, **106**, 247-271, doi: http://dx.doi.org/10.1016/S0016-7061(01)00127-6.

Pisciotto, K.A. 1981. Diagenetic trends in the siliceous facies of the Monterey Shale in the Santa Maria region, California. *Sedimentology*, **28**, 547-571.

1107 Potter, P.E., Maynard, J. & Pryor, W.A. 2012. Sedimentology of shale: study guide and reference
1108 source. Springer Science & Business Media.

1109 Potter, P.E., Maynard, J.B. & Depetris, P.J. 2005. Mud and mudstones: Introduction and overview.
1110 Springer Science & Business Media.

1111 Prêt, D. 2003. *Nouvelles méthodes quantitatives de cartographie de la minéralogie et de la porosité*
1112 *dans les matériaux argileux: application aux bentonites compactées des barrières ouvragées*, CEA,
1113 Grenoble.

1114 Prêt, D., Sammartino, S., Beaufort, D., Fialin, M., Sardini, P., Cosenza, P. & Meunier, A. 2010a. A
1115 new method for quantitative petrography based on image processing of chemical element maps: Part
1116 II. Semi-quantitative porosity maps superimposed on mineral maps. *American Mineralogist*, **95**, 1389-
1117 1398.

1118 Prêt, D., Sammartino, S., Beaufort, D., Meunier, A., Fialin, M. & Michot, L.J. 2010b. A new method
1119 for quantitative petrography based on image processing of chemical element maps: Part I. Mineral
1120 mapping applied to compacted bentonites. *American Mineralogist*, **95**, 1379-1388.

1121 Prior, D.J., Boyle, A.P., Brenker, F., Cheadle, M.C., Day, A., Lopez, G., Peruzzo, L., Potts, G.J.,
1122 Reddy, S. & Spiess, R. 1999. The application of electron backscatter diffraction and orientation
1123 contrast imaging in the SEM to textural problems in rocks. *American Mineralogist*, **84**, 1741-1759.

1124 Pusch, R. 2006. Mechanical properties of clays and clay minerals. *Handbook of Clay Science*, **1**, 247-
1125 260.

1126 Radlinski, A.P., Mastalerz, M., Hinde, A.L., Hainbuchner, M., Rauch, H., Baron, M., Lin, J.S., Fan, L.
1127 & Thiyagarajan, P. 2004. Application of SAXS and SANS in evaluation of porosity, pore size
1128 distribution and surface area of coal. *International Journal of Coal Geology*, **59**, 245-271, doi:
1129 http://dx.doi.org/10.1016/j.coal.2004.03.002.

1130 Rahm, D. 2011. Regulating hydraulic fracturing in shale gas plays: The case of Texas. *Energy Policy*,
1131 **39**, 2974-2981.

1132 Reed, R.M. & Loucks, R.G.A.A.M. 2007. Imaging nanoscale pores in the Mississippian Barnett Shale
1133 of the Northern Ft. Worth Basin. *AAPG Annual Meeting*.

1134 Robinet, J.C., Sardini, P., Coelho, D., Parneix, J.C., Prêt, D., Sammartino, S., Boller, E. & Altmann, S.
1135 2012. Effects of mineral distribution at mesoscopic scale on solute diffusion in a clay-rich rock :
1136 Example of the Callovo-Oxfordian mudstone (Bure, France). *Water Resources Research*, **48**, 1-17.

1137 Rodriguez, R., Crandall, D., Song, X., Verba, C. & Soeder, D. 2014. Imaging Techniques for
1138 Analyzing Shale Pores and Minerals. National Energy Technology Laboratory, Morgantown, WV.

1139 Romero-Sarmiento, M.-F., Rouzaud, J.-N., Bernard, S., Deldicque, D., Thomas, M. & Littke, R. 2014.
1140 Evolution of Barnett Shale organic carbon structure and nanostructure with increasing maturation.
1141 *Organic Geochemistry*, **71**, 7-16, doi: http://dx.doi.org/10.1016/j.orggeochem.2014.03.008.

1142 Ross, D. & Bustin, R.M. 2009. The importance of shale composition and pore structure upon gas
1143 storage potential of shale gas reservoirs. *Marine and Petroleum Geology*, **26**, 916-927, doi:
1144 http://dx.doi.org/10.1016/j.marpetgeo.2008.06.004.

1145 Rouquette, J., Genoud, C., Vazquez-Nin, G.H., Kraus, B., Cremer, T. & Fakan, S. 2009. Revealing
1146 the high-resolution three-dimensional network of chromatin and interchromatin space: a novel
1147 electron-microscopic approach to reconstructing nuclear architecture. *Chromosome research*, **17**, 801-
1148 810.

1149 Roy, S., Raju, R., Chuang, H.F., Cruden, B.A. & Meyyappan, M. 2003. Modeling gas flow through
1150 microchannels and nanopores. *Journal of Applied Physics*, **93**, 4870-4879.

1151 Russ, J.C. 2011. The image processing handbook. CRC press.

Sakellariou, A., Sawkins, T.J., Senden, T.J., Arns, C.H., Limaye, A., Sheppard, A.P., Sok, R.M., Knackstedt, M.A., Pinczewski, W.V., Berge, L.I. & Øren, P.-E. 2003. Micro-CT Facility For Imaging Reservoir Rocks At Pore Scales.

Sammartino, S., Siitari-Kauppi, M., Meunier, A., Sardini, P., Bouchet, A. & Tevissen, E. 2002. An Imaging Method for the Porosity of Sedimentary Rocks: Adjustment of the PMMA Method--Example of a Characterization of a Calcareous Shale. *Journal of Sedimentary Research*, **72**, 937-943.

Saraji, S. & Piri, M. 2015. The representative sample size in shale oil rocks and nano-scale characterization of transport properties. *International Journal of Coal Geology*, **146**, 42-54, doi: http://dx.doi.org/10.1016/j.coal.2015.04.005.

Sardini, P., El Albani, A., Pret, D., Gaboreau, S., Siitari-Kauppi, M. & Beaufort, D. 2009. Mapping and quantifying the clay aggregate microporosity in medium-to coarse-grained sandstones using the 14C-PMMA method. *Journal of Sedimentary Research*, **79**, 584-592.

Sarout, J. & Guéguen, Y. 2008. Anisotropy of elastic wave velocities in deformed shales: Part 2—Modeling results. *Geophysics*, **73**, D91-D103.

Savoye, S., De Windt, L., Beaucaire, C., Bruno, G. & Guitard, N. 2001. Are artificial tracers conservative in argillaceous media? The Tournemire claystone case. *Water-Rock Interaction*, 145-148.

Sayers, C. 1994. The elastic anisotrophy of shales. *Journal of Geophysical Research: Solid Earth*, **99**, 767-774.

Schieber, J. 2010. Common Themes in the Formation and Preservation of Intrinsic Porosity in Shales and Mudstones - Illustrated with Examples Across the Phanerozoic. *Society of Petroleum Engineers Unconventional Gas Conference*, Pittsburgh, Pennsylvania.

Schieber, J., Lazar, R., Bohacs, K., Klimentidis, R.E., Ottmann, J. & Dumitrescu, M. 2012. A Scanning Electron Microscope Study of Porosity in the Eagle Ford Shale of Texas. *In*: AAPG (ed.) *AAPG Annual Convention and Exhibition*. AAPG, Long Beach, California.

Schmitt, L., Forsans, T. & Santarelli, F. 1994. Shale testing and capillary phenomena. *International Journal of Rock Mechanics and Mining Sciences & Geomechanics Abstracts*. Elsevier, 411-427.

Schultz, L.G. 1964. *Quantitative interpretation of mineralogical composition from X-ray and chemical data for the Pierre Shale* Report **2330-7102**.

Scrivener, K.L. & Pratt, P. 1983. Characterization of Portland cement hydration by electron optical techniques. *ELECTRON MICROSCOPY OF MATERIALS., 1983*, **31**, 351-356.

Sealy, C.P., Castell, M.R. & Wilshaw, P.R. 2000. Mechanism for secondary electron dopant contrast in the SEM. *Journal of electron microscopy*, **49**, 311-321.

Shaw, D.B. & Weaver, C.E. 1965. The mineralogical composition of shales. *Journal of Sedimentary Research*, **35**.

Shi, J., Zhang, L., Li, Y., Yu, W., He, X., Liu, N., Li, X. & Wang, T. 2013. Diffusion and Flow Mechanisms of Shale Gas through Matrix Pores and Gas Production Forecasting. *SPE Unconventional Resources Conference Canada*. Society of Petroleum Engineers.

Silin, D. & Kneafsey, T.J. 2012. Shale Gas: Nanometer-Scale Observations and Well Modelling. doi: 10.2118/149489-pa.

Slatt, R.M. 2011. Important Geological Properties of Unconventional Resource Shales. *Central European Journal of Geosciences*, **3**, 435-448, doi: DOI 10.2478/s13533-011-0042-2.

Slatt, R.M. & O'Brien, N.R. 2011. Pore types in the Barnett and Woodford gas shales: Contribution to understanding gas storage and migration pathways in fine-grained rocks. *AAPG Bulletin*, **95**, 2017.

1196 Sok, R.M., Knackstedt, M.A., Varslot, T., Ghous, A., Latham, S. & Sheppard, A.P. 2010. Pore Scale
1197 Characterization of Carbonates At Multiple Scales: Integration of Micro-CT, BSEM, And FIBSEM.
1198 *PetroPhysics*, **51**.

1199 Sondergeld, C.H., Ambrose, R.J., Rai, C.S. & Moncrieff, J. 2010a. Micro-Structural Studies of Gas
1200 Shales. *Petroleum Engineers Unconventional Gas Conference*, Pittsburgh, Pennsylvania.

1201 Sondergeld, C.H., Ambrose, R.J., Rai, C.S. & Moncrieff, J. 2010b. Micro-structural studies of gas
1202 shales. *SPE Unconventional Gas Conference*. Society of Petroleum Engineers.

1203 Sondergeld, C.H., Newsham, K.E., Comisky, J.T., Rice, M.C. & Rai, C.S. 2010c. Petrophysical
1204 Considerations in Evaluating and Producing Shale Gas Resources. *SPE Unconventional Gas*
1205 *Conference*. Society of Petroleum Engineers.

1206 Sondergeld, C.H., Rai, C.S. & Curtis, M.E. 2013. Relationship Between Organic Shale Microstructure
1207 and Hydrocarbon Generation. *SPE Unconventional Resources Conference-USA*. Society of
1208 Petroleum Engineers.

1209 Sopp, O. 1900. X-RADIOGRAPHY AS A GEOTECHNICAL TOOL. *Norwegian Geotechnical*
1210 *Institute Publ*.

1211 Stauber, M. & Müller, R. 2008. Micro-computed tomography: a method for the non-destructive
1212 evaluation of the three-dimensional structure of biological specimens. *Osteoporosis*. Springer, 273-
1213 292.

1214 Stock, S. 1999. X-ray microtomography of materials. *International Materials Reviews*, **44**, 141-164.

1215 Suganuma, T. 1985. Measurement of surface topography using SEM with two secondary electron
1216 detectors. *Journal of electron microscopy*, **34**, 328-337.

1217 Tariq, F., Lee, P., Haswell, R. & McComb, D. 2011. The influence of nanoscale microstructural
1218 variations on the pellet scale flow properties of hierarchical porous catalytic structures using
1219 multiscale 3D imaging. *Chemical Engineering Science*, **66**, 5804-5812.

1220 Taylor, K. & Macquaker, J. 2014. Diagenetic alterations in a silt-and clay-rich mudstone succession:
1221 an example from the Upper Cretaceous Mancos Shale of Utah, USA. *Clay minerals*, **49**, 213-227.

1222 Tian, H., Pan, L., Xiao, X., Wilkins, R.W., Meng, Z. & Huang, B. 2013. A preliminary study on the
1223 pore characterization of Lower Silurian black shales in the Chuandong Thrust Fold Belt, southwestern
1224 China using low pressure N 2 adsorption and FE-SEM methods. *Marine and Petroleum Geology*, **48**,
1225 8-19.

1226 Timur, A., Hempkins, W. & Weinbrandt, R. 1971. Scanning electron microscope study of pore
1227 systems in rocks. *Journal of Geophysical Research*, **76**, 4932-4948.

1228 Tissot, B. 1984. Recent advances in petroleum geochemistry applied to hydrocarbon exploration.
1229 *AAPG Bulletin*, **68**, 545-563.

1230 Tissot, B., Durand, B., Espitalie, J. & Combaz, A. 1974. Influence of nature and diagenesis of organic
1231 matter in formation of petroleum. *AAPG Bulletin*, **58**, 499-506.

1232 Tissot, B., Pelet, R. & Ungerer, P. 1987. Thermal history of sedimentary basins, maturation indices,
1233 and kinetics of oil and gas generation. *AAPG Bulletin*, **71**, 1445-1466.

1234 Tiwari, P., Deo, M., Lin, C.L. & Miller, J.D. 2013. Characterization of oil shale pore structure before
1235 and after pyrolysis by using X-ray micro CT. *Fuel*, **107**, 547-554, doi:
1236 http://dx.doi.org/10.1016/j.fuel.2013.01.006.

1237 Torsaeter, M., Vullum, P.E. & Nes, O.-M. 2012. Nanostructure vs. Macroscopic Properties of Mancos
1238 Shale. *SPE Canadian Unconventional Resources Conference*. Society of Petroleum Engineers,
1239 Calgary, Alberta, Canada.

1240 Tosaya, C.A. 1982. Acoustical properties of clay-dearing rocks. Dept. of Geophysics, School of Earth
1241 Sciences.

Trager, E.A. 1924. Kerogen and its relation to the origin of oil. *AAPG Bulletin*, **8**, 301-311.

Vasin, R.N., Wenk, H.R., Kanitpanyacharoen, W., Matthies, S. & Wirth, R. 2013. Elastic anisotropy modeling of Kimmeridge shale. *Journal of Geophysical Research: Solid Earth*, **118**, 3931-3956.

Vassoyevich, N., Korchagina, Y.I., Lopatin, N. & Chernyshev, V. 1970. Principal phase of oil formation. *International Geology Review*, **12**, 1276-1296.

Vega, B., Ross, C.M. & Kovscek, A.R. 2014. Imaging-Based Characterization of Calcite-Filled Fractures and Porosity in Shales. *Unconventional Resources Technology Conference (URTEC)*. Society of Petroleum Engineers.

Vergès, J.M. & Morales, J.I. 2014. The gigapixel image concept for graphic SEM documentation. Applications in archeological use-wear studies. *Micron*, **65**, 15-19.

Vik, B., Bastesen, E. & Skauge, A. 2013. Evaluation of representative elementary volume for a vuggy carbonate rock—Part: Porosity, permeability, and dispersivity. *Journal of Petroleum Science and Engineering*, **112**, 36-47, doi: http://dx.doi.org/10.1016/j.petrol.2013.03.029.

Wellington, S. & Vinegar, H. 1987. X-ray computerized tomography. *Journal of Petroleum Technology*, **39**, 885-898.

Williams, D.B. & Carter, C.B. 1996. The transmission electron microscope. Springer.

Withers, P.J. 2007. X-ray nanotomography. *Materials Today*, **10**, 26-34, doi: http://dx.doi.org/10.1016/S1369-7021(07)70305-X.

Wu, P. & Aguilera, R. 2012. Investigation of Gas Shales at Nanoscale Using Scan Electron Microscopy, Transmission Electron Microscopy and Atomic Force Microscopy. *SPE Annual Technical Conference and Exhibition*. Society of Petroleum Engineers, San Antonio, Texas, USA.

Yaalon, D. 1961. Mineral composition of the average shale.

Yoo, T.S. 2004. Insight into images. *AK Peters*.

Yoon, H. & Dewers, T.A. 2013. Nanopore structures, statistically representative elementary volumes, and transport properties of chalk. *Geophysical Research Letters*, **40**, 4294-4298.

Yven, B., Sammartino, S., Géraud, Y., Homand, F. & Villiéras, F. 2007. Mineralogy, texture and porosity of Callovo-Oxfordian argillites of the Meuse/Haute-Marne region (eastern Paris Basin). *Mémoires de la Société géologique de France*, **178**, 73-90.

Zhang, S., Klimentidis, R.E. & Barthelemy, P. 2012. Micron to millimeter upscaling of shale rock properties Based on 3D imaging and modeling. *Exxomobil Upstream Research Co., Houston, Tx, USA. VSG-Visualisation Sciences Group, Burlinton, MA, USA*.

Zou, C., Jin, X., Zhu, R., Gong, G., Sun, L., Dai, J., Meng, D., Wang, X., Li, J. & Wu, S. 2015. Do Shale Pore Throats Have a Threshold Diameter for Oil Storage? *Scientific reports*, **5**.

Abbreviations

2D = Two-dimensional

3D = Three-dimensional

EM = Electron Microscopy

SEM = Scanning Electron Microscopy

BSE = Back-Scatter Electron

SE = Secondary Electron

ESEM = Environmental SEM

EDX = Energy Dispersive X-ray spectroscopy

TEM = Transmission Electron Microscopy

3D-EM = Three-Dimensional Electron Microscopy

FIB = Focused Ion Beam

BIB = Broad Ion Beam

SBF-SEM = Serial Block-Face Scanning Electron Microscopy

XCT = X-ray Computed Tomography

TOC = Total Organic Carbon

XRD = X-Ray Diffraction

EBSD = Electron Back-Scatter Diffraction

REV = Representative Elementary Volume

VOI = Volume of interest

PPL = Plain Polarized Light

XPL = Cross Polarised Light